

Flood Impacts on Net Ecosystem Exchange in the Midwestern and Southern United States in 2019

Nikolay V. Balashov^{1,2}, Lesley E. Ott¹, Brad Weir^{1,3}, Sourish Basu^{1,2}, Kenneth
J. Davis^{4,5}, Natasha L. Miles⁴, Anne M. Thompson^{6,7}, Ryan M. Stauffer⁶

¹NASA Global Modeling and Assimilation Office (GMAO), Goddard Space Flight Center, Greenbelt, MD,
20771, USA

²Earth System Science Interdisciplinary Center, University of Maryland, College Park, MD, USA

³Goddard Earth Sciences Technology and Research, Universities Space Research Association, 7178
Columbia Gateway Drive, Columbia, MD, 21046, USA

⁴Department of Meteorology and Atmospheric Science, The Pennsylvania State University, University
Park, PA 16802, USA

⁵Earth and Environmental Systems Institute, The Pennsylvania State University, University Park, PA
16802, USA

⁶Earth Sciences Division, NASA Goddard Space Flight Center, Greenbelt, MD, 20771, USA

⁷University of Maryland-Baltimore County, JCET, Baltimore, MD 21228

Key Points:

- A devastating flood occurred in 2019 over the Midwestern and Southern regions of the US significantly affecting ecosystem carbon cycling
- Net ecosystem exchange is examined in the flood-affected areas with NASA's GEOS modeling system from 2017 through 2019
- The 2019 floods caused a net reduction in Midwestern crop carbon uptake and smaller net increase in non-crop uptake in Southern states

Corresponding author: Nikolay V. Balashov, nikolay.v.balashov@nasa.gov

Abstract

Climate extremes such as droughts, floods, heatwaves, frosts, and windstorms add considerable variability to the global year-to-year increase in atmospheric CO₂ through their influence on terrestrial ecosystems. While the impact of droughts on terrestrial ecosystems has received considerable attention, the response to flooding is not well understood. To improve upon this knowledge, the impact of the 2019 anomalously wet conditions over the Midwest and Southern US on CO₂ vegetation fluxes is examined in the context of 2017-2018 when such precipitation anomalies were not observed. CO₂ is simulated with NASA's Global Earth Observing System (GEOS) combined with the Low-order Flux Inversion, where fluxes of CO₂ are estimated using a suite of remote sensing measurements including greenness, night lights, and fire radiative power as well as with a bias correction based on insitu observations. Net ecosystem exchange CO₂ tracers are separated into the three regions covering the Midwest, South, and Eastern Texas and adjusted to match CO₂ observations from towers located in Iowa, Mississippi, and Texas. Results indicate that for the Midwestern region consisting primarily of corn and soybeans crops, flooding contributes to a 15-25% reduction of annual net carbon uptake in 2019 in comparison to 2017 and 2018. These results are supported by independent reports of changes in agricultural activity. For the Southern region, comprised mainly of non-crop vegetation, annual net carbon uptake is enhanced in 2019 by about 10-20% in comparison to 2017 and 2018. These outcomes show the heterogeneity in effects that excess wetness can bring to diverse ecosystems.

Plain Language Summary

Carbon dioxide (CO₂) is the main driver of climate change whose atmospheric concentration is governed by a mix of human emissions and absorption by land and ocean sinks. Understanding how these sinks will respond to climate change in the future, including in response to increasingly frequent extreme events like floods, is critical in setting reliable emission reduction targets and improving Earth system models. Here, the devastating flood of 2019 that affected the Midwestern and Southern US is examined with respect to its effects on the ability of land ecosystems to absorb CO₂. The analysis is performed using NASA's GEOS model, which simulates CO₂ concentrations based on a simple land model that had previously been adjusted to match global background insitu observations. In this study, fluxes are adjusted using CO₂ observations from measurement towers in the U.S. Simulations covering the years of 2017-2019 are compared and indicate that parts of the affected region absorbed less CO₂ in 2019 than in previous years. The results demonstrate the effects of floods on the carbon cycle are complex and warrant further study, which is needed to understand how land ecosystems will respond to climate change in the future.

1 Introduction

Understanding the future evolution of the carbon cycle is crucial to improve climate change predictions (Frank et al., 2015). Studies show that climate extremes (i.e., extreme weather events) have a noticeable effect on terrestrial ecosystems influencing the cycling of carbon and thereby affecting global atmospheric CO₂ concentrations (Reichstein et al., 2013; Frank et al., 2015). These extremes are characterized by meteorological phenomena such as droughts, floods, heat waves, frosts, and windstorms (Reichstein et al., 2013). While general understanding regarding how these extremes affect the global carbon cycle exists, each case presents a unique challenge that may deviate from expected behavior. To better understand the effects of climate extremes on carbon exchange between terrestrial ecosystem and atmosphere, detailed analysis of relevant case studies is required.

72 Droughts are common extreme weather events that impact terrestrial ecosystem
73 carbon processes and are relatively well studied (van der Molen et al., 2011). In the time
74 of drought, the ability of an ecosystem to consume CO₂ decreases (Frank et al., 2015;
75 Schwalm et al., 2012). While the impact of droughts on terrestrial ecosystem has received
76 considerable attention over the recent years, the response of an ecosystem to flooding
77 events is intricate and ambiguous (Zaerr, 1983; Miyata et al., 2000; Knapp et al., 2008;
78 Dušek et al., 2009; Zona et al., 2012; Dalmagro et al., 2019). As the climate changes, cli-
79 mate models predict an increase in precipitation for midlatitude regions, thereby increas-
80 ing the likelihood of flooding events affecting these ecosystems (Knapp et al., 2008; Zhang
81 & Villarini, 2021). Therefore, it is imperative to better understand how the potential in-
82 crease in flooding events may affect future carbon budget.

83 The effects of flooding on carbon exchange in the terrestrial ecosystem depends on
84 the type of vegetation affected. Wetlands tend toward storing less atmospheric carbon
85 during flooding as photosynthesis weakens; however, annual Net Ecosystem Exchange
86 (NEE) may not change much as ecosystem respiration (RE) also decreases (Han et al.,
87 2015). Typically, during a growing season trees, shrubs, and grasses support net uptake
88 of atmospheric CO₂ and continue to do so during moderate flooding, but it is not ex-
89 actly clear how an increase in the magnitude of the flooding may alter this process (Kramer
90 et al., 2008; Bourtsoukidis et al., 2014; Detmers et al., 2015). Ma et al. (2016) found that
91 grasslands in Australia can even benefit from anomalously wet conditions and assimilate
92 more carbon compared to normal soil moisture conditions. Croplands, however, are
93 easily susceptible to waterlogging and tend to be a net source of atmospheric carbon when
94 flooding occurs (Rosenzweig et al., 2002; Ahmed et al., 2013; Yin et al., 2020; Yildirim
95 & Demir, 2022). Although the majority of CO₂ that is initially absorbed by croplands
96 is eventually released back into the atmosphere, the cropland soils have the capacity to
97 sequester atmospheric CO₂ and their ability to hold carbon is critically important for
98 reducing global atmospheric CO₂ levels (Paustian et al., 2000; Follett, 2001; Zomer et
99 al., 2017). Also, extreme precipitation events may cause topsoil erosion leading to ad-
100 ditional carbon emissions into the atmosphere (Hilton et al., 2008; Dinsmore et al., 2013;
101 Lal, 2019). To further the knowledge of the effects of flooding on ecosystem carbon fluxes,
102 the spring/early summer Midwestern and central Southern US anomalously wet condi-
103 tions of 2019 are investigated.

104 Heavy precipitation in the spring/early summer of 2019 resulted in widespread flood-
105 ing of the Upper Mississippi River Basin and the surrounding regions causing damages
106 in the range of 2-3 billion US dollars (Neri et al., 2020; Reed et al., 2020; Price & Berkowitz,
107 2020). The focus of this study is on the Midwest (M) and the South (S and T, Figure
108 1), where anomalously wet conditions affected areas with different types of vegetation.
109 Stream gauges levels along with variety of other data and survey reports indicate that
110 the M region experienced periods of major flooding while the regions S and T were only
111 partially affected (supporting information section S1). In the Midwest vegetation pri-
112 marily consists of croplands such as maize (corn) and soybeans, while in the South there
113 are mainly forests transitioning to prairies in Eastern Texas (Figure 1). The primary aim
114 of this study is to investigate the impact of the 2019 anomalously wet conditions on the
115 NEE with simulations from NASA's Goddard Earth Observing System (GEOS) Low-
116 order Flux Inversion (LoFI) model in the affected regions, in contrast to the years 2017
117 and 2018 which experienced comparatively lower anomalous precipitation levels, and to
118 assess results in the context of the regional GEOS LoFI NEE climatology from the pe-
119 riod 2000-2016.

120 Previously, Yin et al. (2020) showed the ability to quantify Midwest atmospheric
121 CO₂ and Midwest croplands gross primary production (GPP) anomalies during the above-
122 mentioned 2019 flood using XCO₂ measurements from the Orbiting Carbon Observa-
123 tory 2 (OCO-2) and solar-induced chlorophyll fluorescence (SIF) derived from the TRO-
124 Pospheric Monitoring Instrument (TROPOMI). Comparing 2019 to 2018, their results

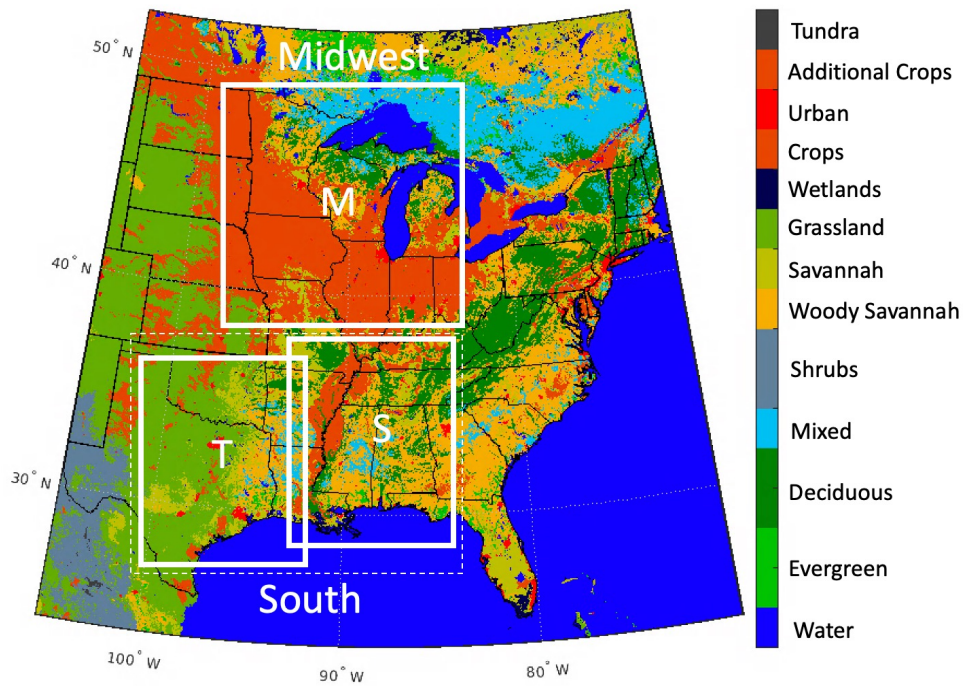


Figure 1. Land cover map of the Eastern Conterminous United States (CONUS) derived from Moderate Resolution Imaging Spectroradiometer (MODIS). White rectangles indicate regions affected by the anomalous precipitation and are the focus of this study. Capital letter M indicates the Midwest region, while capital letters S (South) and T (Texas) represent regions of the South (for more details see Data and Methods section).

125 suggest a reduction in the Midwest cropland GPP of -0.21 PgC in June and July and
 126 partial recovery of 0.14 PgC in August and September. Additionally, they noted a flood-
 127 forced 3-week delay in the planting date of crops across much of the area. Turner et al.
 128 (2021) also used TROPOMI SIF to study the impacts of the 2019 flood on CONUS veg-
 129 etation arriving at similar conclusions as Yin et al. (2020) with 2018 as a reference year.

130 The present study builds upon Yin et al. (2020) and Turner et al. (2021) by an-
 131 alyzing optimized GEOS LoFI NEE of the flood-affected region over the period 2017-
 132 2019 using insitu tower data and extending the comparison to GEOS LoFI 2000-2016
 133 regional NEE climatology. The focus is on better understanding of the 2019 precipita-
 134 tion event and its impact on the affected ecosystems from the perspective of the atm-
 135 spheric carbon monitoring system. Specifically, the study looks at monthly and annual
 136 regional optimized NEE budgets for years 2017-2019 comparing them to the GEOS LoFI
 137 2000-2016 NEE budget climatology. The key scientific inquiry at hand is determining
 138 the extent to which the 2019 late spring/early summer flood in the Midwest and parts
 139 of the South has impacted the annual NEE budget, and whether this impact is signifi-
 140 cant enough to be observable with the tools employed. Additionally, the performance
 141 of the NASA near real time carbon modeling tool, GEOS LoFI, is assessed and impli-
 142 cations for carbon monitoring are discussed.

143 2 Data and Methods

144 2.1 MERRA-2

145 To map out regions of the flooding in 2019, precipitation, root zone soil wetness,
 146 and 2-m temperature data from the Modern-Era Retrospective analysis for Research and
 147 Applications, Version 2 (MERRA-2) are used (Gelaro et al., 2017). Bias corrected MERRA-
 148 2 precipitation (mm) comprised of background data products [such as Goddard Earth
 149 Observing System Model, version 5 (GEOS-5) or Forward Processing system for Instru-
 150 ment Teams (FP-IT)] and observations [i.e., Global Precipitation Climatology Project
 151 (GPCP)] is utilized (Reichle, Draper, et al., 2017; Reichle, Liu, et al., 2017). Root zone
 152 soil wetness is described by the ground wetness variable for the 0-100 cm layer of soil.
 153 The variable is dimensionless in units of relative saturation ranging from 0 to 1, where
 154 value of 1 indicates completely saturated soil. Root zone soil wetness, precipitation, and
 155 2-m temperature May-August 2017-2019 anomalies with respect to May-August 1981-
 156 2010 climatology are calculated over the region of interest.

157 2.2 Crop Data

158 Since croplands contribute significantly to the carbon cycle of the M region, 2017-
 159 2019 United States Department of Agriculture (USDA) crop planting data are analyzed
 160 for corn (maize) and soybeans - the two most common crops in the US Midwest. In this
 161 study, three attributes, which are crop planting progress, acres planted, and grain yield
 162 of corn and soybeans from years 2017-2019 are compared. The following states are an-
 163 alyzed here: Illinois, Indiana, Iowa, Kansas, Michigan, Minnesota, Missouri, Nebraska,
 164 Ohio, South Dakota, and Wisconsin. The data is taken from National Agriculture Statis-
 165 tics Service provided by USDA (<https://quickstats.nass.usda.gov/>).

166 2.3 CO₂ Data

167 2.3.1 Optimization Data

168 The optimization of the GEOS model (described later in section 2.6) takes place
 169 in two different areas, the Midwest (M) and the South (broken down into two regions:
 170 S and T, Figure 1). The process of optimization consists of adjusting GEOS NEE CO₂
 171 tracers from the 3 regions (M, S, and T) over the 3 years (2017-2019) in an attempt to

172 match 5-day running mean of daily observations [averaged over the afternoon hours of
 173 1500-1700 local standard time (LST)] from insitu CO₂ towers located in the regions of
 174 interest: West Branch, Iowa (WBI) in M, Magee, Mississippi (MS-01) in S, Grenada, Mis-
 175 sissippi (MS-02) in S, and Moody, Texas (WKT) in T (see Figure 2).

176 The WBI tower is in the agricultural ecosystem (corn belt) of eastern Iowa and is
 177 part of the National Oceanic and Atmospheric Administration (NOAA) Earth System
 178 Research Laboratories/Global Monitoring Laboratory (ESRL/GML) tall tower network
 179 that is tasked with the goal of long-term carbon-cycle gas monitoring in the atmospheric
 180 boundary layer (ABL) of continental areas (Andrews et al., 2014; Schuldt et al., 2021).
 181 The location of the tower is ideal for CO₂ monitoring pertinent to the Midwestern crop-
 182 lands and hence is used here to analyze the effects of the 2019 flooding.

183 MS-01 and MS-02 towers are in Mississippi and were instrumented initially for the
 184 Gulf Coast Intensive, designed to characterize CO₂ in the southeastern region of the US
 185 and maintained through 2019 as part of the airborne Atmospheric Carbon and Trans-
 186 port - America (ACT-America) project (Miles et al., 2018). The MS towers did not mea-
 187 sure CO₂ simultaneously; therefore, to represent CO₂ of the S region, MS-01 is used for
 188 2017 and MS-02 is used for 2018-2019. These towers are well suited for this study as the
 189 state of Mississippi did see significant wet anomalies in 2019 but avoided major flood-
 190 ing that occurred upstream of the state.

191 Finally, WKT represents the T region of the South. Like WBI, the tower is part
 192 of the NOAA ESRL/GML tall tower network (Andrews et al., 2014). The location of
 193 the tower is optimal for capturing CO₂ variability in eastern Texas and western Louisiana,
 194 where the flooding of 2019 was also partially present.

195 **2.3.2 Validation Data**

196 Validation process with tower-based and airborne measurements is aimed at de-
 197 termining how well the towers used for the optimization act as a proxy for the regions
 198 of interest. The M region is validated with the Indianapolis Flux Experiment (INFLUX)
 199 background tower 1 that is located on the southwestern part of Indianapolis, the direc-
 200 tion least influenced by the CO₂ emissions from the city (Davis et al., 2017). As in Iowa
 201 (where WBI is located), vegetation in Indiana mainly consists of crops, making it a good
 202 choice for the validation of the model optimizations at WBI. However, INFLUX tower
 203 1 is immediately surrounded by forests, in contrast to WBI. The S and T regions are val-
 204 idated using towers in Millerville, Alabam (AL-01) and Monroe, Louisiana (LA-01). To
 205 be consistent with the optimization, 5-day running mean of daily observations (averaged
 206 over the afternoon hours of 1500-1700 LST) is utilized.

207 The 2019 ACT-America campaign is also used for validation. ACT-America is an
 208 airborne NASA Earth Venture mission dedicated to improving the accuracy, precision,
 209 and resolution of atmospheric inverse estimates of CO₂ and CH₄ sources and sinks on
 210 a regional scale (Davis et al., 2021). The mission conducted 5 seasonal campaigns (in-
 211 cluding 2 summer campaigns) over the 2016-2019 period. For each campaign two air-
 212 craft (C-130 and B-200) were used to survey three different regions in the United States:
 213 The South, the Midwest, and the Mid-Atlantic. Data from the 2019 campaign covering
 214 the South and the Midwest is used, which occurred in June and July of 2019. Most of
 215 the flights took place in the period of 1100-1700 LST. For validation purposes the bound-
 216 ary layer [\sim 330 m above ground level (AGL)] CO₂ was averaged for each of the selected
 217 flight days.

218 **2.4 GEOS Model Configuration Including LoFI Flux Package**

219 NASA GEOS general circulation model, constrained by MERRA-2 meteorology fields,
 220 with resolution of 0.5 by 0.625 degrees and 72 vertical layers (Molod et al., 2015) is uti-

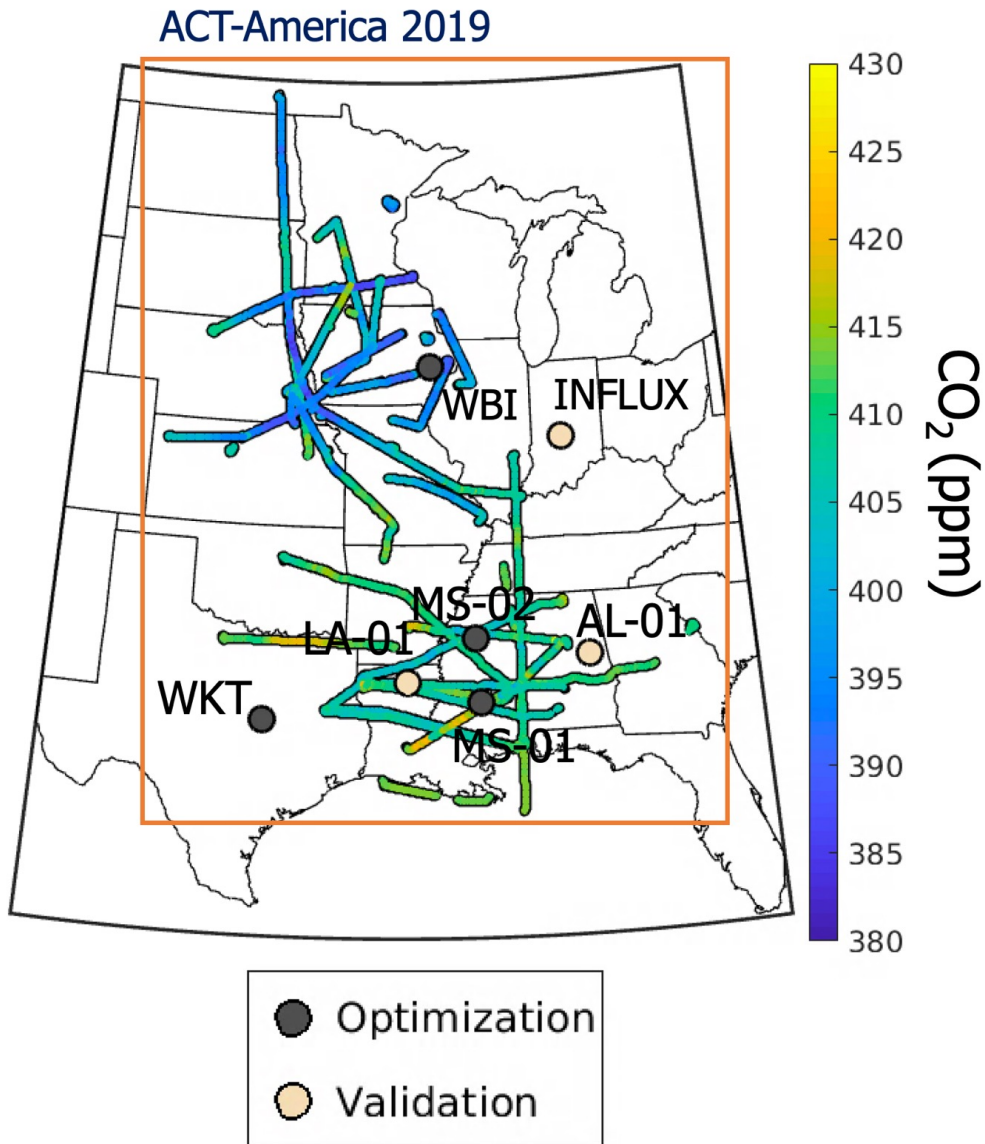


Figure 2. Observations that are used for the GEOS model optimization and validation. Aircraft transect mole fractions are shown inside the ABL and are used for validation. Towers are labeled by circles.

221 lized to simulate CO₂ over the region of interest from January 14th to December 14th
 222 for the years 2017-2019 (Weir et al., 2021). It includes the Low-order Flux Inversion (LoFI)
 223 package, which contains a compilation of carbon fluxes driven by remote-sensing land
 224 surface data (Ott et al., 2015; Weir et al., 2021) and a bias correction process designed
 225 to reproduce CO₂ mole fractions observed at NOAA’s in situ network. There are five com-
 226 ponents to the mentioned LoFI flux package: NEE, biomass burning, fossil fuel combustion,
 227 tion, ocean exchange, and an empirical land sink (bias correction of the fluxes).

228 NEE is computed using the Carnegie-Ames-Stanford Approach – Global Fire Emis-
 229 sions Dataset version 3 (CASA-GFED 3; Randerson et al., 1996; van der Werf et al., 2010)
 230 that estimates carbon fluxes using satellite-derived vegetation products and MERRA-
 231 2 meteorology. Biomass burning CO₂ emissions are derived with the Quick Fire Emis-
 232 sions Dataset (QFED; Koster et al., 2015), which is constructed using MODIS fire ra-
 233 diative power (FRP) estimates in near real-time. Fossil fuel combustion is provided by
 234 the Open-source Data Inventory for Anthropogenic CO₂ (ODIAC; Oda & Maksyutov,
 235 2015; Oda et al., 2018) that is based on disaggregated country-level fossil fuel CO₂ emis-
 236 sion inventories using a global power plant database and satellite observations of night-
 237 time lights. Ocean exchange of CO₂ is estimated using the differences between the par-
 238 tial pressure of CO₂ in seawater (pCO₂^{sw}) derived from the Takahasi et al. (2009) cli-
 239 matology and the partial pressure in the atmosphere (pCO₂^{atm}) taken from the NOAA
 240 marine boundary layer (MBL) reference (Masarie & Tans, 1995; Dlugokencky & Tans,
 241 2016). An empirical land sink is applied as a bias correction to the collection of fluxes
 242 to constrain the modeled atmospheric CO₂ growth with the observed growth rates de-
 243 rived from the NOAA MBL reference (Weir et al., 2021). The empirical sink matches
 244 the global total fluxes for a year to a specified atmospheric growth rate of CO₂ by re-
 245 ducing heterotrophic respiration during months when there is an increase in the 2-m air
 246 temperature, which is used as an approximate indicator of soil temperature, compared
 247 to the previous month.

248 In addition to using LoFI as a driver of GEOS CO₂ simulation, it is also used to
 249 compute 2000-2016 monthly and annual NEE climatology that could be used as a sup-
 250 plemental metric for comparison to initial and optimized 2017-2019 NEE. Monthly 2000-
 251 2016 NEE climatology is computed by averaging the sum of 3-hourly NEE values for each
 252 month (except January and December) over the 17 years and annual climatology is com-
 253 puted by summing all 3-hourly NEE values for each year and then finding an average
 254 of these 17 sums. Due to the way the model is ran, for January 3-hourly values from the
 255 dates of 18th through 31st are summed and for December 3-hourly values from the dates
 256 of 1st through 14th are summed. Furthermore, monthly spatial NEE 2017-2019 anoma-
 257 lies of regions M, S, and T with respect to spatial monthly 2000-2016 NEE climatology
 258 are computed (supporting information section S6).

259 2.5 Definition of Tagged Tracer Regions

260 Before the optimization an area that influences towers is designated using NOAA’s
 261 Hybrid Single-Particle Lagrangian Integrated Trajectory (HYSPPLIT) model backward
 262 trajectories (Stein et al., 2015). The trajectories are released backwards for every 6 hours
 263 for May through September of 2019 at the three optimization towers WBI, MS-02 (it is
 264 assumed MS-02 is representative of MS-01), and WKT from the level of the correspond-
 265 ing sensor (121-379 m AGL) using the North American Regional Reanalysis (NARR)
 266 meteorology. The approximate area influencing each tower combined with the MODIS
 267 Land Cover Climate Modeling Grid Product (MCD12C1) allow for the generation of CO₂
 268 mole fraction tracer masks applied to tag regional NEE within GEOS that can be then
 269 used in the optimization (Figure 3). MCD12C1 is the reprojection of the tiled MODIS
 270 Land Cover Type Product (MCD12Q1) with the sub-pixel proportions of each land cover
 271 class in each 0.05° pixel and the aggregated quality assessment information from the In-
 272 ternational Geosphere-Biosphere Programme (IGBP) scheme (Sulla-Menashe & Friedl,

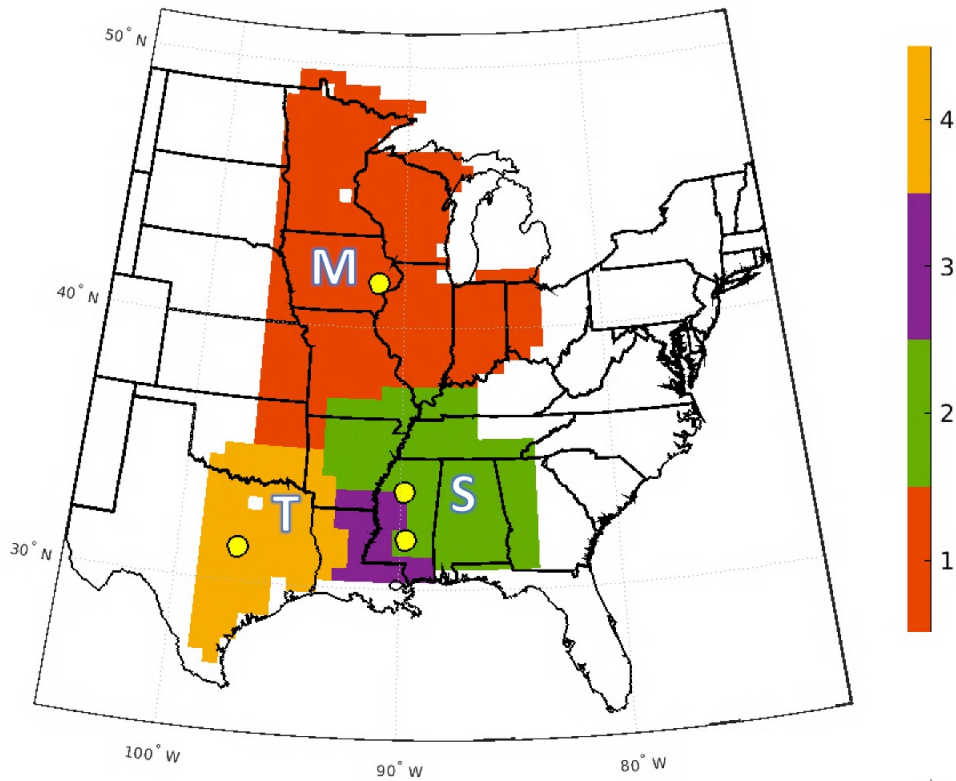


Figure 3. Masks for the optimization based on the backward HYSPLIT trajectories, where red region 1 influences WBI tower in Iowa and is labeled as M NEE CO₂ tracer, the green region 2 influences MS-01 and MS-02 towers in Mississippi and is labeled as S NEE CO₂ tracer, the purple region 3 influences both MS and WKT towers (part of both S and T NEE CO₂ tracers), and finally the yellow region 4 influences WKT tower in Texas and is labeled as T NEE CO₂ tracer. Yellow circles indicate towers used for optimization.

273 2018). MCD12C1 is used to generate the appropriate masks of vegetation areas of inter-
 274 est while removing any urban and coastal environments.

275 2.6 Optimization Approach

276 To quantify the effects of 2019 flooding on regional vegetation, NEE is compared
 277 to the years 2017 and 2018. Though NEE is available from the LoFI flux package, it is
 278 possible that these fluxes are inaccurate because of the use of a highly simplified diag-
 279 nostic vegetation model. To provide a better estimate, the NEE component of the LoFI
 280 collection, representative of the vegetation fluxes of a given area, is adjusted to minimize
 281 the model-observation CO₂ mole fraction difference. The optimization is independently
 282 performed for the three different regions of M, S, and T (Figure 3), where each region
 283 is characterized by its individual NEE CO₂ tracer based on the selected insitu towers.

284 The observed CO₂ mole fraction can be expressed in the following way:

$$285 \quad CO_{2,obs} = CO_{2,model} + \Delta CO_2, \quad (1)$$

286 where $CO2_{model}$ represents CO_2 from GEOS and ΔCO_2 is the mole fraction of CO_2 that
 287 needs to be added to the modeled mole fraction to arrive at the observed value. The $CO2_{model}$
 288 term can be expanded as

$$289 \quad CO2_{model} = CO2_{ini} + CO2_{ocn} + CO2_{FF} + CO2_{fire} + CO2_{NEE}, \quad (2)$$

290 where $CO2_{ini}$ is an initial condition that consists of all the accumulated CO_2 at a par-
 291 ticular model grid cell in the model prior to January 14th of a given year (either 2017,
 292 2018, or 2019) and the rest of the right-hand terms are additions from ocean (OCN), fos-
 293 sil fuels (FF), fire, and NEE. In the current work it is hypothesized that NEE term is
 294 the most uncertain and that the ΔCO_2 term in equation (1) is mainly driven by the $CO2_{NEE}$
 295 term. Therefore, it is the only term adjusted to bring the modeled CO_2 closer to the ob-
 296 served CO_2 . The $CO2_{NEE}$ tracer is tracked by the model from the selected regions and
 297 the rest of the globe as shown in Figure 3 and can be expressed as

$$298 \quad CO2_{NEE} = CO2_{NEE}^M + CO2_{NEE}^S + CO2_{NEE}^T + CO2_{NEE}^{global}, \quad (3)$$

299 with the right hand terms representing regional and the rest of the globe NEE CO_2 trac-
 300 ers. Only the regional tracers are adjusted in this study.

301 The optimization is performed at each of the three towers (M, S, and T) by solv-
 302 ing for the minimum value of the cost function (Rodgers, 2000):

$$303 \quad J(a) = \frac{1}{2} [(\hat{y} + \alpha CO2_{NEE}^{region}) - y] R^{-1} [(\hat{y} + \alpha CO2_{NEE}^{region}) - y]^T + \frac{1}{2} \alpha B^{-1} \alpha^T, \quad (4)$$

304 where α is a scaling factor by which NEE need to be changed, \hat{y} is modeled 5-day run-
 305 ning mean of daily afternoon (1500-1700 LST) averages of CO_2 , y is observed 5-day run-
 306 ning mean of daily afternoon (1500-1700 LST) averages of CO_2 , B is the scaling factor
 307 error covariance term, and R is the observation-model error covariance matrix. B can
 308 be a matrix if more than one tracer is optimized, but in the current case of optimizing
 309 just one tracer, B becomes equivalent to $\sigma_{\alpha_p}^2 = 0.5$, which determines by how much the
 310 scaling factor α can be adjusted from the initial scaling factor $\alpha_p = 0$. The value of 0.5
 311 is empirically derived and in this case is just large enough to allow for physically reason-
 312 able NEE variation. R matrix represents combined observation-model error as well as
 313 the covariances among the days in each segment. The adjustment is performed on a to-
 314 tal of 22 segments consisting of 15 daily y and \hat{y} values to smooth out NEE daily vari-
 315 ability over the time of about 2 weeks (Friend et al., 2007; Chevallier et al., 2012). Square
 316 matrix R is generated by first calculating observation-model daily error terms ε with the
 317 expression (Heald et al., 2004):

$$318 \quad \varepsilon = y - \hat{y} - \overline{y - \hat{y}}. \quad (5)$$

319 Then ε terms are divided into 22 segments consisting of consecutive 15 daily values from
 320 the total of m daily values (in this case total is 330 days comprising most of the year).
 321 Variance is calculated for each segment as follows,

$$322 \quad \sigma_i^2 = \frac{(\sum_{i=1}^{15} \varepsilon_i)^2}{15 - 1}. \quad (6)$$

323 This variance is unique to each segment and repeated for every day inside of an individ-
 324 ual segment. Afterwards, the variance is converted to standard deviation σ (by taking
 325 a square root) and the initial version of R is

$$R = \begin{bmatrix} \sigma_1^2 & r_{12}\sigma_1\sigma_2 & \dots & r_{1m}\sigma_1\sigma_m \\ r_{21}\sigma_2\sigma_1 & \sigma_2^2 & \dots & r_{2m}\sigma_2\sigma_m \\ \vdots & \vdots & \ddots & \vdots \\ r_{m1}\sigma_m\sigma_1 & r_{m2}\sigma_m\sigma_2 & \dots & \sigma_m^2 \end{bmatrix}, \quad (7)$$

where the covariance terms representing propagation of error in time are modified by coefficient

$$r_{ij} = e^{-|i-j|/d}, \quad (8)$$

with d being a time scale. After the completion of the initial optimization, R is adjusted using reduced χ^2 statistic when initial term α becomes available for every segment with 22 being the total number of optimized segments,

$$\chi^2 = \frac{1}{22}[(\hat{y} + \alpha CO2_{NEE}^{region}) - y]R^{-1}[(\hat{y} + \alpha CO2_{NEE}^{region}) - y]^T. \quad (9)$$

For each segment, σ is modified until reduced χ^2 approximately approaches a value of 1 and final value of α is determined.

The error covariance of α is estimated with

$$\hat{R} = [(CO2_{NEE}^{region})^T R^{-1} CO2_{NEE}^{region} + B^{-1}]^{-1}. \quad (10)$$

Once α is estimated, it is used to construct an optimized time series of CO_2 mole fractions along with its variation based on the estimated vector \hat{R} (which provides 22 values of $\sigma_{optimized}$) by randomly drawing 1000 times from the normal distribution in the following fashion,

$$\alpha^* = \alpha + Normal(0, \sigma_{optimized}). \quad (11)$$

Then α and α^* are used to generate optimized CO_2 time series with the corresponding noise:

$$CO2_{optimized} = CO2_{model} + \alpha CO2_{NEE}^{region}, \quad (12)$$

$$CO2_{optimized}^* = CO2_{model} + \alpha^* CO2_{NEE}^{region}. \quad (13)$$

Afterwards, the adjusted NEE is estimated by summing the LoFI NEE (NEE_{model}^{region}) over all the pixels of each region (M, S, and T) in 15-day increments and then using

$$NEE_{optimized}^{region} = NEE_{model}^{region} + \alpha NEE_{model}^{region}. \quad (14)$$

The optimized NEE for each month is computed by summing the appropriate derived increments. For January, dates of 18th through 31st are used for the summation and for December dates of 1st through 14th are summed. The total annual NEE is found by adding all the 22 increments of each year. The uncertainties of 15-day segments are represented by the variance values from the \hat{R} and uncertainties of the monthly and annual NEE are found by summing corresponding variances.

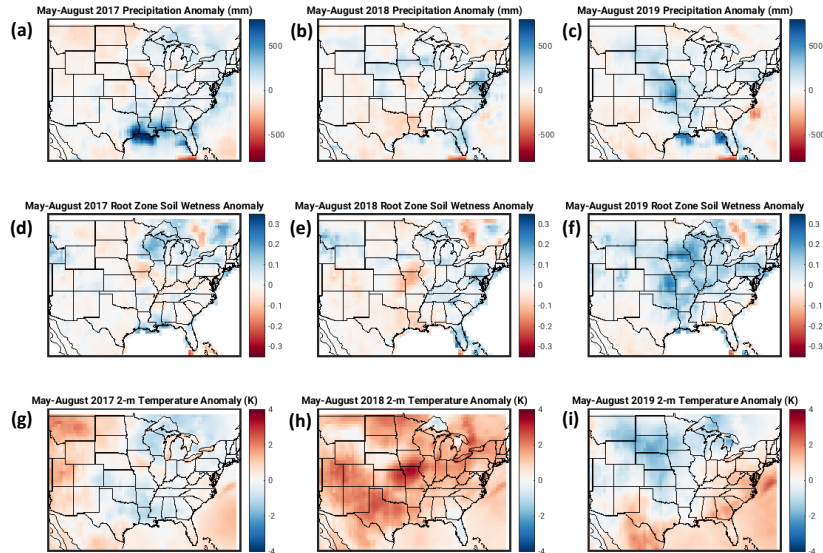


Figure 4. Precipitation, root zone soil wetness, and 2-m temperature August-May anomalies with respect to 1981-2010 climatology from MERRA-2 (Gelaro et al., 2017) in the eastern and central US for years 2017-2019, where panels (a), (b), and (c) correspond to precipitation anomalies over 2017-2019, panels (d), (e), and (f) correspond to root zone soil wetness over 2017-2019, and panels (g), (h), and (i) correspond to 2-m temperature anomalies over 2017-2019.

356 3 Results and Discussion

357 3.1 Relevant meteorology and its effects on crops

358 Figure 4 shows precipitation, root zone soil wetness, and 2-m temperature anomalies
 359 for the eastern and central US over the years of 2017-2019 during the period of May-
 360 August when most of the 2019 flooding and its effects occurred. Comparing May-August
 361 precipitation totals over the years 2017-2019 indicate that 2019 (Figure 4c) saw notice-
 362 able wet anomalies in the central US including the Midwest and the South with the Mid-
 363 west experiencing much of the flooding and the South only being partially affected (more
 364 information about the flood is in the supporting information section S1). The same re-
 365 gions in 2017 and 2018 (Figures 4a and 4b) generally saw negative anomalies except for
 366 coastal regions of southeastern Texas, southern Louisiana, southern Mississippi, and south-
 367 ern Alabama in 2017, when extremely wet conditions occurred. More evidence of the 2019
 368 flood can be gleaned from the widespread root zone soil wetness positive anomalies in
 369 May-August of 2019 (Figure 4f) in comparison to May-August of 2017 and 2018 (Fig-
 370 ures 4d and 4e), although some slightly positive anomalies can be seen in Wisconsin and
 371 coastal gulf states in 2017. Surface (2-m) temperature anomalies over May-August in
 372 2019 are mostly below normal in the Midwest and close to normal values in the eastern
 373 regions, while in May-August of 2018 whole shown area except for Florida is well-above
 374 average, and 2017 in general is unremarkable.

375 The immediate effects of 2019 flooding on the two major US crops is evident from
 376 Figure 5, where in Figures 5a and 5b planned planting of corn and soybeans is delayed
 377 by almost a month. The delay is likely caused by the severe waterlogging that occurred
 378 in early May not allowing farmers to proceed with the planned crop planting timetables.
 379 Figures 5c and 5d indicate that the total planted annual acres of corn and soy are about

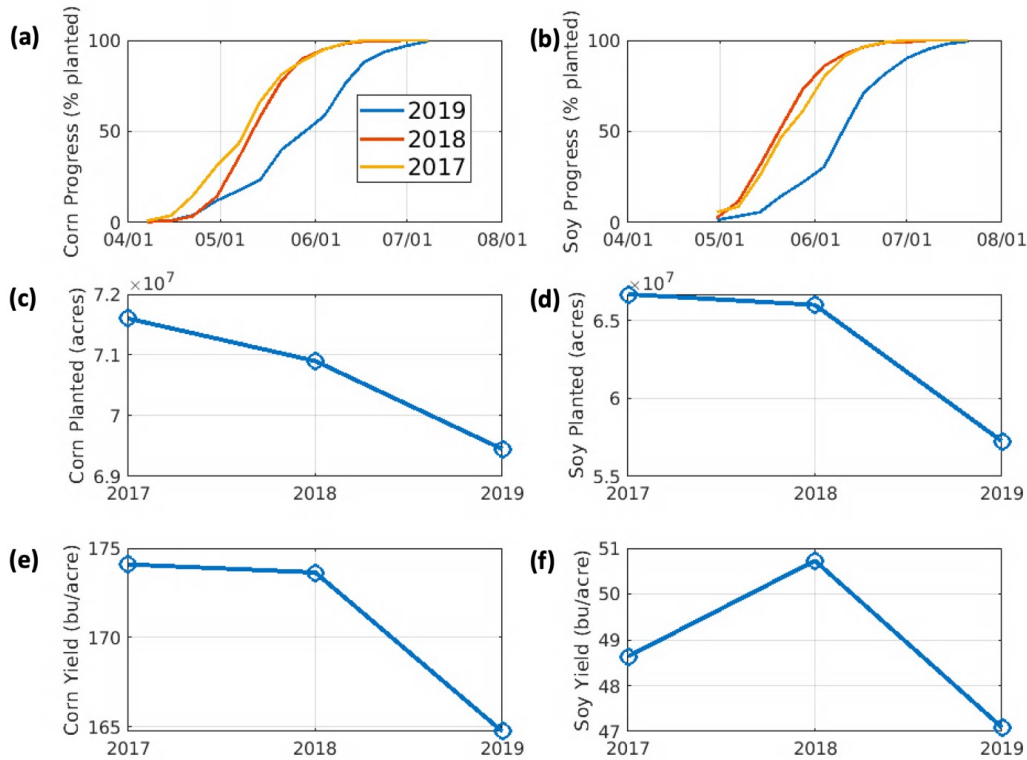


Figure 5. Corn and soybean statistics in the Midwestern states (listed in section 2.2) showing progress (percent planted), acres planted, and yield for the years 2017-2019, where (a), (c), and (e) indicate the mentioned statistics for corn and (b), (d), and (f) for soy (<https://quickstats.nass.usda.gov/>).

380 3-15% lower in 2019 than in years 2017 and 2018. Figures 5e and 5f show both corn and
 381 soy yields are lower in 2019 in comparison to 2017 and 2018.

382 These results are also partially supported by Figure S3 exhibiting Fraction of Photo-
 383 synthetically Active Radiation (FPAR) anomalies for years 2017-2019. FPAR indicates
 384 plant’s ability to incorporate solar radiation to promote its growth (more details are in-
 385 cluded in supporting information section S2; Los et al., 2000). The figure shows notice-
 386 able negative FPAR anomalies in parts of the Midwest over 2019 suggesting that the flood
 387 is significant enough to affect plant function and to cause pronounced reduction of crop
 388 yields in the Midwest compared to years 2017 and 2018. This may imply that the amount
 389 of carbon assimilated by the crops is also lower in 2019 than in the two prior years. This
 390 hypothesis as well as the possible opposite effects of the anomalously wet conditions on
 391 the non-crop vegetation (positive FPAR anomalies in the S and T regions) is addressed
 392 in the next section.

393 3.2 NEE Optimization in the Midwest and the South

394 In Figure 6, the results of the optimization process are presented by comparing the
 395 optimized GEOS CO₂ time series with the original non-optimized GEOS CO₂ time se-
 396 ries and the tower observations. Uncertainty of the optimization is denoted by grey lines
 397 representing one sigma variation. The time series are 5-day running daily means plot-
 398 ted as the days of year at the regions M, S, and T over the years 2017-2019. The adjust-
 399 ments made because of the optimization process (explained in section 2.6) are illustrated

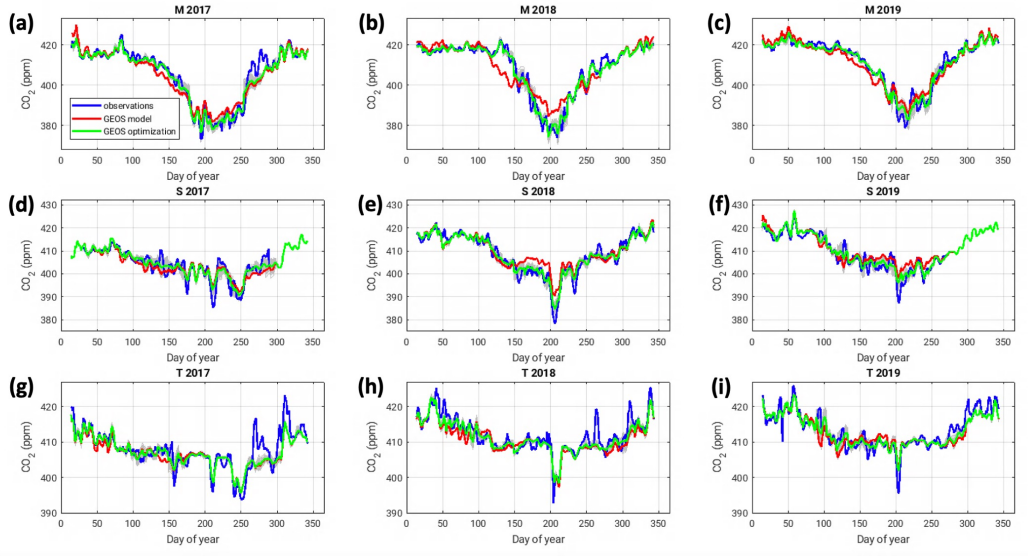


Figure 6. CO₂ insitu observations vs. GEOS model along with its optimization for towers WBI, MS (1 and 2), and WKT located in M, S, and T regions, where (a) WBI in 2017, (b) WBI in 2018, (c) WBI in 2019, (d) MS-01 in 2017, (e) MS-02 in 2018, (f) MS-02 in 2019, (g) WKT in 2017, (h) WKT in 2018, (i) WKT in 2019.

400 in Figure 7, which shows 9 time series of the resultant scaling factors for GEOS NEE CO₂
 401 tracer mole fractions reflecting the time series shown in Figure 6. The scaling factors in
 402 Figure 7 are plotted in a such way that positive values indicate a need to increase up-
 403 take in the model, while negative values indicate a need to decrease uptake in the model.
 404 Scaling factor uncertainty of one sigma is indicated by black lines.

405 Beginning with the analysis of CO₂ cycle in the M region (Figures 6a-c), growing
 406 seasons differ for each of the years with 2017 having the earliest drawdown start day on
 407 about 100th day of the year as evident from Figure 6a. The model picks up this feature
 408 in 2017 generally well, but with incorrect magnitude. The years 2018 and 2019 exhibit
 409 slightly later drawdown start days with 2019 experiencing the beginning of the net up-
 410 take earlier than 2018 by about 10-20 days. For both years the model erroneously pre-
 411 dictes the start of growing season around the day 100. The peak period of net uptake lasts
 412 about 20-30 days longer in 2017 compared to 2018, and only a few days longer compared
 413 to 2019. Overall, the model performs adequately in replicating the shape of the draw-
 414 down cycle; however, during the peak net uptake period, it appears to exhibit a deficiency
 415 in the necessary uptake.

416 Upon further examination of the model’s performance in the M region, it is dis-
 417 covered that during the three-year period, scaling factors shown in Figures 7a-c demon-
 418 strate comparable characteristics, although with variations in magnitude. The princi-
 419 pal trends of GEOS LoFI model biases in region M are identified as insufficient uptake
 420 during the first 50 days, excessive uptake between days 100-170, inadequate uptake from
 421 around day 170 to approximately day 230, elevated uptake from roughly day 250 to day
 422 300, and insufficient uptake during the remainder of the year. The year 2018 necessitates
 423 the most significant optimization adjustments, particularly within the period spanning
 424 from day 100 to approximately day 220.

425 Possible explanations for some of the observed variations in drawdown cycle in the
 426 M region can be found in Figure 4. From a meteorological perspective, there are no re-

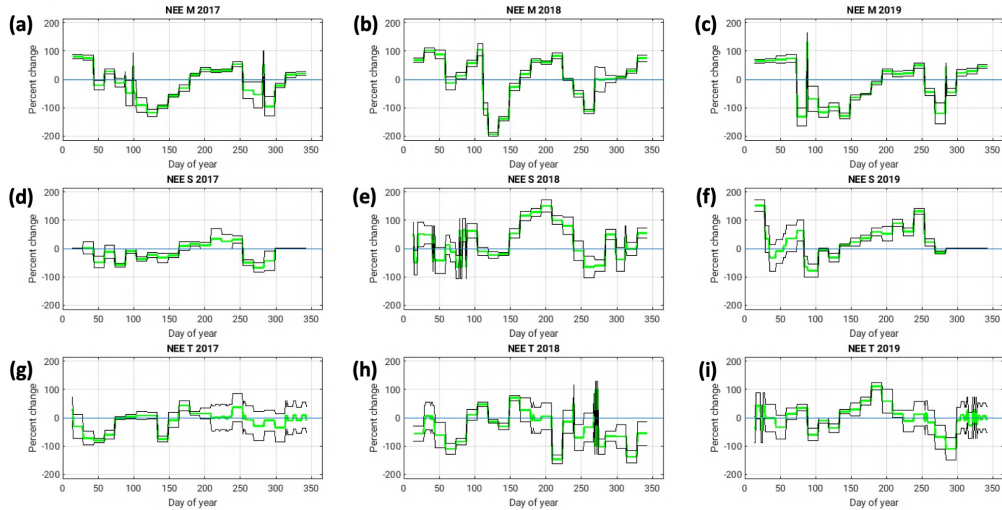


Figure 7. Scaling factors (shown in green) in percentages of GEOS NEE CO₂ tracer mole fractions as a function of day of year using towers WBI, MS (1 and 2), and WKT located in M, S, and T regions, where (a) WBI in 2017, (b) WBI in 2018, (c) WBI in 2019, (d) MS-01 in 2017, (e) MS-02 in 2018, (d) MS-02 in 2019, (g) WKT in 2017, (h) WKT in 2018, (i) WKT in 2019. Black lines indicate one sigma interval of an overall uncertainty of an estimated scaling factor. The scaling factors are plotted in such a way as to indicate a decrease in carbon uptake when the scaling factor is negative and to indicate an increase in carbon uptake when the scaling factor is positive.

427 markable anomalies observed in the Midwest region during 2017, while the years 2018
 428 and 2019 exhibit anomalous levels of heat and precipitation, respectively. During the peak
 429 of growing season between May and August, Figure 4h reveals widespread positively anomalous
 430 2-m temperatures encompassing the Midwest region in 2018. Also Figure 4e hints
 431 at some deficit in root zone soil wetness in some of the central states. These meteorological
 432 parameters indicate that spring and summer of 2018 experienced partial drought
 433 conditions, which led to a slight setback in corn progress (Figure 5a) delaying drawdown
 434 cycle. The year 2019 witnessed extreme flooding because of the above-normal precipitation
 435 illustrated in Figure 4c, and substantially increased root zone soil wetness as demonstrated
 436 in Figure 4f. These anomalously wet conditions impeded the growth of corn and
 437 soybean, as indicated in Figures 5a and 5b, consequently reducing carbon uptake.

438 Moving on to the S region (Figures 6d-f), where the model generally tracks accurately
 439 tower observations except for a period in 2018 where it is too high. The growing
 440 season is much less defined in the S region than in the region M making it difficult to
 441 state exactly how it differs among the shown years. The drawdown begins earlier in the
 442 S region than in the M region by about 20-30 days. Additionally, the S region CO₂ time
 443 series exhibit an interesting feature in the form of noticeable jaggedness, which reflects
 444 variations in air masses. During summer, air moving from the north tends to be depleted
 445 in CO₂ as it passes over the widespread crop areas, resulting in dips in the time series
 446 (Figure S4). Conversely, air moving from the south tends to be enriched in CO₂ as it
 447 accumulates over the Gulf of Mexico, leading to spikes in the time series. In winter, CO₂
 448 tends to pile up along a frontal boundary introducing spikes in CO₂ tower observations
 449 over the southern areas (Figures S5). Such spikes are also produced by spring frontal intrusions
 450 as higher-CO₂ air is brought to the South (where a growing season has already

started) from the Midwest where the switch from efflux to uptake did not yet occur (Figure S6).

The scaling factors derived from the optimization for the S region shown in Figures 7d-f share a few important similarities although also contain differences. All three years indicate a need for more uptake in the GEOS LoFI from about day 150 to about day 250. The time series markedly differ in magnitude of the scaling factors with 2017 showing the least amount of variation and 2018 with the most dramatic bias peaking at about 150%.

Meteorologically, the S region is slightly less affected by the temperature anomalies in 2018 and the root zone soil wetness anomalies in 2019; however, the mentioned features are still found in Figures 4h and 4f. Also, a large amount of coastal precipitation in 2017, evident from Figure 4a, makes year 2017 potentially atypical. It is difficult to make any conclusions about how the weather specifically affected vegetation carbon uptake in the S region over the years 2017-2019, but a little more analysis on this is presented in section 3.4.

The T region is characterized by mostly consistent CO₂ time series with a slight hint of growing season beginning to occur early in a year, interspersed with occasional sharp drops and spikes (Figure 6g-i), similar to what is observed in the S region. The NEE tracer derived from GEOS LoFI does not exhibit large values in the T region and therefore does not allow for much optimization. The model generally does a decent job predicting CO₂, but it consistently fails at identifying peaks of CO₂ suggesting challenges associated with carbon arriving from other areas.

In the T region, the scaling factors tend to be noisy, varying up and down, except for a period in 2019 from day 150 to day 200 where it is positive suggesting the need for more net carbon uptake in GEOS LoFI. The overall oscillatory nature of the scaling factor in the T region reflects the savanna/grasslands vegetation of the T region corresponding to the smaller values of NEE tracer that are hard to adjust effectively in comparison to the M and S regions.

3.3 Optimization Validation

In this study, the validation is meant to gauge the tower representativeness of each respective region by evaluating determined adjustments of the GEOS simulation using independent-from-optimization observations. The scaling factors derived at the optimization sites in all the 3 regions are combined and used to adjust CO₂ values at every validation site. The optimization described in the previous section is validated with 3 towers INFLUX, LA-01, and AL-01 and with data from the 2019 airborne ACT-America campaign. INFLUX tower results are demonstrated in the Figures 8a-c, where 5-day running daily averages of the observed, modeled, and model-adjusted CO₂ are plotted over a year. Comparing Figures 6a-c and Figures 8a-c indicates that the GEOS model bias is generally similar for both WBI and INFLUX towers although with different magnitudes – too much uptake in the first part of the growing season (days 100-160) and too little uptake at the heart of the drawdown (days 170-230). This result is reasonable as Indiana, like Iowa, is mainly an agriculture state (Figure 1). Therefore, the NEE optimization corrections (shown in green) adjust the model in the right direction. However, it is likely that the different vegetation in the proximity of INFLUX tower 1 (forests) and a somewhat different transport influence area affect the local CO₂ mole fractions.

Next, validation performed at LA-01 tower in years 2017 and 2018 is illustrated in Figures 8d and 8e. Validation at this tower serves to verify optimizations in both regions S and T. For the most part validation time series tend to line up well with observations demonstrating that MS-1, MS-2, and WKT towers are well representative of the S and T regions. The near-perfect alignment of optimized and observed values during days 150-

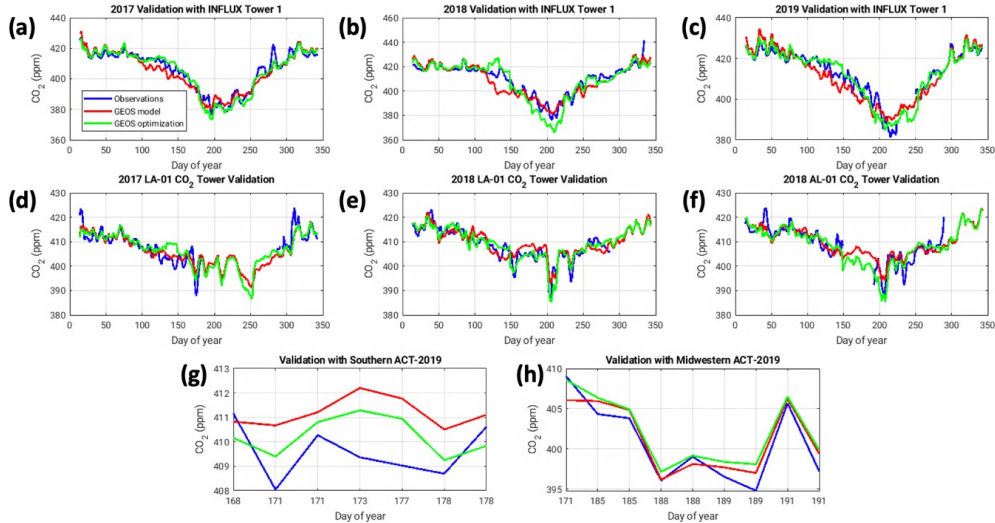


Figure 8. Validation of the optimization using various datasets throughout the years of interest, where the INFLUX tower 1 is shown in (a-c) for years 2017-2019, LA-01 tower is shown in (d-e) for years 2017-2018, AL-01 tower is shown in (f) for year 2018, southern ACT-2019 daily averaged flights are shown in (g), and Midwestern ACT-2019 daily averaged flights are shown in (h).

200, as illustrated in Figure 8e, is particularly impressive. Unfortunately, a significant portion of the observed data is missing in 2017. Also, it is possible to see that the correction of days 136-150 for 2017 (Figure 8d) is inconsistent with the Louisiana data. This discrepancy may imply that although the T and S regions share similarities they are not identical.

The only data that is available from the AL-01 tower is for 2018 and at that it is incomplete. The AL-01 tower can partially validate the S region optimization. Figure 8f shows that in the days 120-150 optimization is not helpful, but later in the period (starting at about day 210) some improvement can be noted confirming higher carbon uptake. In this regard 2018 LA-01 and AL-01 towers are consistent and support the evidence of too little uptake in the GEOS LoFI system at the peak of growing season.

Finally, airborne ACT-America 2019 campaign is used to validate the optimizations. ACT-America focused on all the regions of interest, first in the S and T regions during the second half of June (days 168-178) and then in the M region during the first part of July (days 185-191). Figure 8g compares airborne CO_2 averages to corresponding original and adjusted model values. Noticeable improvement can be seen in the adjusted model, signaling that the S and T regions likely did experience higher carbon uptake than the original GEOS calculation showed. Regarding ACT-America flights in the M region denoted in Figure 8h, the original and adjusted models do not differ by much and generally closely resemble the airborne measurements. This is not surprising as Figure 7c suggests that in early July of 2019 (days 185-191) the model accurately estimated CO_2 mole fractions not requiring substantial adjustment.

Overall, the process of validating the optimizations showed that the derived scaling factors from the towers can be extended to the regions of interest albeit at times with a considerable error, which is difficult to quantify precisely. Established GEOS biases based on the WBI tower in the M region are partially observed at INFLUX tower 1. Re-

gional ACT-America 2019 flights in the M region also indicate that the optimizations are reasonable. With regards to the S and T regions, towers LA-01 and AL-01 in 2018 and corresponding ACT-America 2019 flights show improved agreements with adjusted model fields. On the other hand, the LA-01 tower in 2017 does not suggest much improvement; however, those are limited fragments of the overall validation dataset. Additionally, Figures S7 and S8 demonstrate a reverse process (supporting information section S4), where validation sites are used to solve for the regions M, S, and T providing consistent results to the ones obtained in the current section.

3.4 Regional Annual NEE Variability

Once the optimization and validation procedures are accomplished it is possible to adjust GEOS NEE over all the regions and compare the outcomes among the years 2017-2019 as well as 2000-2016 LoFI climatology. Figure 9 presents a comparison of the monthly and annual original, adjusted, and climatological GEOS NEE for the M region, spanning the years 2017-2019. Figure 9a reflects Figure 6a, where 2017 begins to exhibit growing season sometime in April-May as optimized NEE is hovering around 0 Pg C. The growing season ends in October when net carbon source becomes apparent. Year 2018, as described in section 3.2 (Figure 6b), displays a notably later inception to a growing season. Optimized NEE implies that net uptake begins sometime in June and ends in October (Figures 9b). The delay of the growing season in 2018 is likely a result of the drought conditions (Haigh et al., 2022). Another interesting feature that could be spotted in 2018 is a drastic net uptake in July (Figure 9b), which can be explained by the fact that most of the crops in 2018 experienced an earlier than average blooming stage leading to a higher than usual net uptake in July but lower than usual net uptake in September. Although in the analysis of the optimized time series it appeared that 2019 had a delayed start to a growing season, Figure 9c seems to suggest that in terms of carbon uptake 2019 behaves similarly to 2017 in April-May despite experiencing the flood. It is only later in the growing season that 2017 is able to assimilate more carbon than the growing season of 2019 implying that if 2017 can be considered a normal year the impact of flooding on NEE was not instantaneous but delayed. However, determining whether 2017 qualifies as a typical year is not a simple matter (supporting information S6). As pointed out in section 3.2, optimized NEE for all the 3 years conveys that non-optimized GEOS has not enough uptake in July and August.

An assessment of NEE yearly totals for the M region (Figure 9d) shows that 2019 has the smallest NEE compared to 2017 and 2018 supporting the assertion that the 2019 flood did reduce annual carbon uptake in the M region; however, the actual reduction in net uptake mainly occurred in June and July of 2019. The climatological LoFI NEE is close to the 2019 value indicating that the effect of this flooding on annual carbon budget is not as unusual. However, it is important to note that the GEOS LoFI climatology is likely biased as it is based on the CASA model product that is known to underestimate carbon uptake over the US Midwestern croplands (Y. Zhou et al., 2020).

The overall growing season magnitude of NEE in the S region (Figures 10a-c) is approximately four times lower than that of the M region. It is hypothesized here that this difference between M and S regions can be explained by the switch of vegetation from mostly crops to mixed forests and savannas (Figure 1). Crops such as corn and soybean that are abundant in the M region exhibit more efficient GPP with relatively less attendant RE than many other plant types (Guanter et al., 2014). Comparing GPP and RE outputs from GEOS LoFI between regions M and S in 2019 leads to similar conclusions (Figure S9). According to the examined 3 years and climatology the growing season in the S region appears to be from April to September-October. In 2017 the optimization does not significantly alter GEOS model fluxes, while noticeable changes are observed in 2018 and 2019. In years 2018 and 2019 the optimization implies that carbon uptake in the S region should be noticeably higher than what the original GEOS simulation in-

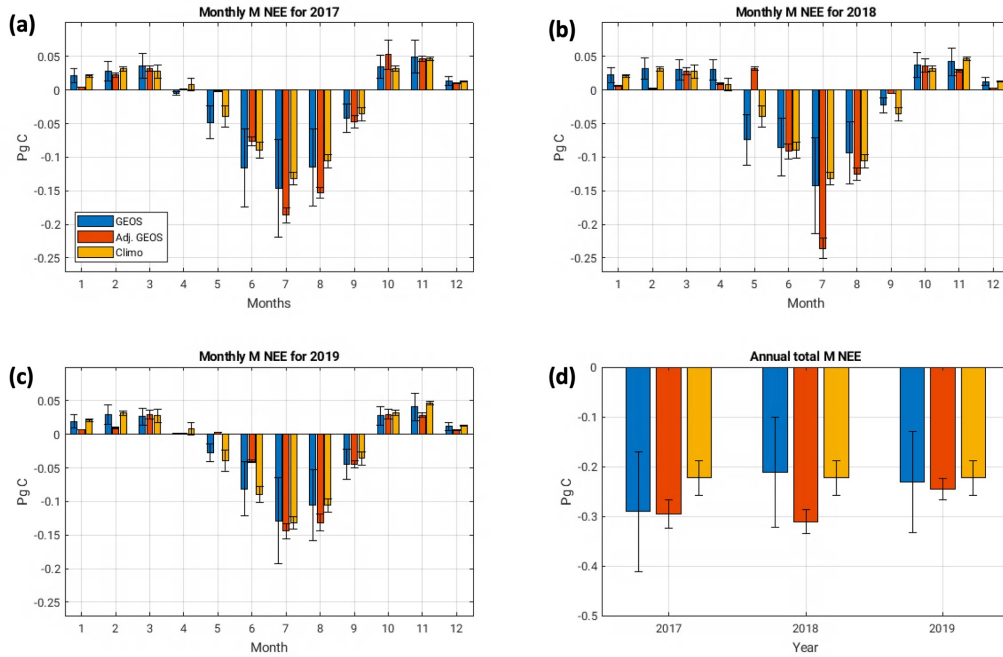


Figure 9. Original, adjusted, and climatological (2000-2016) GEOS NEE (in Pg of carbon) in the M region, where (a-c) panels show monthly flux for years 2017-2019 and (d) summarizes annual NEE flux for years 2017-2019. The uncertainty is one sigma.

579 dicates. That is especially true of 2018, where the annual uptake is increased by about
 580 50% after the adjustment. Out of all the examined years, 2019 reveals the highest an-
 581 nual carbon uptake in the S region as evident from Figure 10d. This may indicate that
 582 the above-average rainfall of 2019 (Figure 4c) along with near or slightly above normal
 583 2-m temperatures (Figure 4f) enhanced the regional plant growth, which is reflected by
 584 the higher than typical CO_2 drawdown. Climatological values of NEE tend to lack up-
 585 take from mid to late summer in comparison to 2017-2019 optimized values (Figures 10a-
 586 c) implying potential systematic bias in GEOS LoFI.

587 The T region can be characterized by an even smaller NEE annual variability in
 588 comparison to M and S regions reflecting the local vegetation consisting of grasslands
 589 and savannas (Figure 1). Figures 11a-c imply shifted growing seasons from those in the
 590 regions M and S lasting from about March to early August. Although GEOS LoFI is gen-
 591 erally in agreement with the optimization, it tends to show a net uptake that is too high
 592 during April and May. An interesting feature can be noted in Figure 11b, where Septem-
 593 ber of 2018 exhibits relatively high net source of carbon in both GEOS LoFI and opti-
 594 mization. This could be potentially explained by the anomalously wet September that
 595 occurred that year in the region (National Centers for Environmental Information, 2018).
 596 The Figure S10 indicates that RE rate surpassed GPP rate during September 2018 in
 597 the T region, which suggests that extreme precipitation significantly contributed to the
 598 net source of atmospheric carbon. In Figure 11d, 2018 has the least negative NEE likely
 599 attributable to the unseasonably warm conditions during the summer (Figure 4h) and
 600 extreme flooding in early fall. On the other hand, 2019 looks like a completely normal
 601 year for the T region with annual carbon budget being near identical to the 2000-2016
 602 regional climatology. Indeed, Figures 4c and 4f show that root zone soil wetness and pre-
 603 cipitation fields are near normal in Texas for May-August period in 2019.

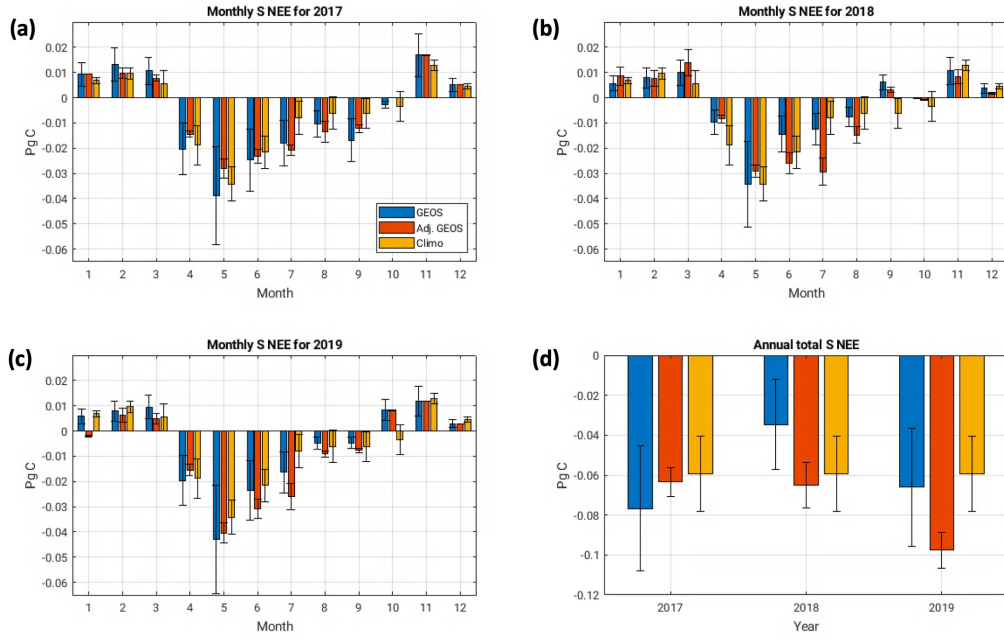


Figure 10. Original, adjusted, and climatological (2000-2016) GEOS NEE (in Pg of carbon) in the S region, where (a-c) panels show monthly flux for years 2017-2019 and (d) summarizes annual NEE flux for years 2017-2019. The uncertainty is one sigma.

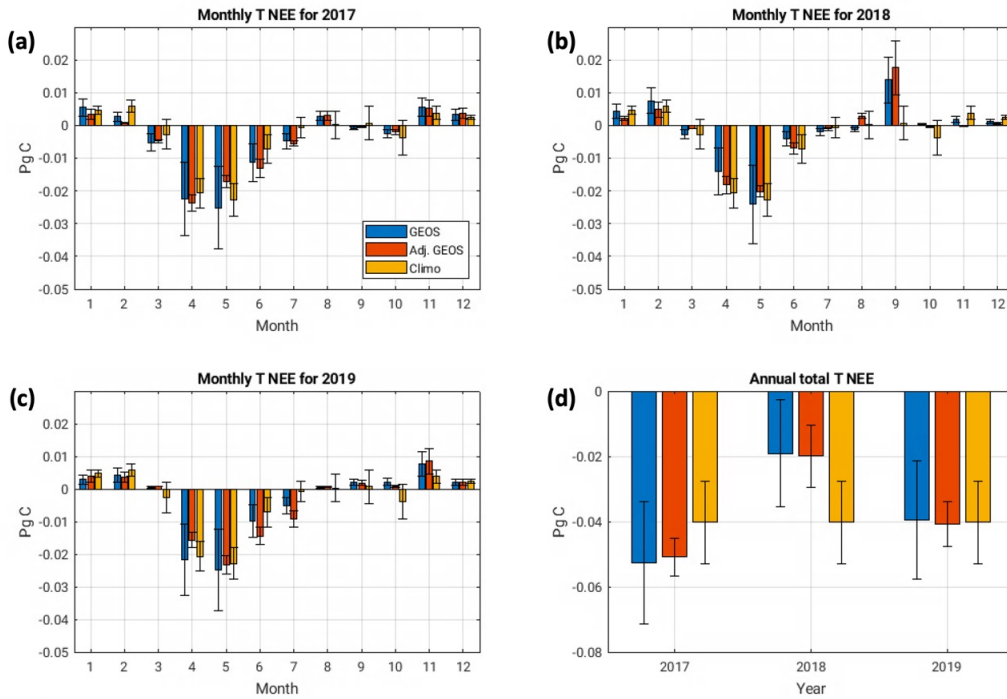


Figure 11. Original, adjusted, and climatological (2000-2016) GEOS NEE (in Pg of carbon) in the T region, where (a-c) panels show monthly flux for years 2017-2019 and (d) summarizes annual NEE flux for years 2017-2019. The uncertainty is one sigma.

604 As an additional exploration, section S6 in supporting information examines spa-
605 tial anomalies of NEE, GPP, and RE from the GEOS LoFI model (Figures S11, S12, and
606 S13) and contrasts them against adjusted spatial NEE anomalies (Figure S14). All of
607 the calculated anomalies are based on the LoFI 2000-2016 climatology and therefore should
608 be treated with caution as the climatology itself is likely biased. This is supported by
609 the optimization results shown in Figures 9-11. The bias is also evident in Figure S14
610 where generally for all the years it can be observed that May and June tend to have too
611 much carbon uptake while July and August too little [with the exception of July 2019
612 (Figure S11c), which is being affected by the flood]. Such consistent anomalies make it
613 difficult to separate actual anomalies from the GEOS LoFI biases, but it could be con-
614 cluded with a high measure of confidence that GEOS LoFI overpredicts NEE in the first
615 part of the growing season and under predicts NEE in the second half of the growing sea-
616 son. Interestingly, it is difficult to point out which NEE component is responsible for such
617 a bias at any given situation as Figures S12 and S13 do not suggest consistent variations
618 between GPP and RE indicating the complexity of the issue.

619 3.5 Effects of 2019 Flooding on NEE

620 After examining the annual variability of NEE at the M, S, and T regions for both
621 2017-2019 and the 2000-2016 LoFI climatology, it is now possible to contextualize the
622 effects of the 2019 flooding on NEE within a broader perspective. The most significant
623 impacts on NEE are apparent in the M and S regions, where the annual NEE budgets
624 for 2019 stand out in contrast to years 2017-2018. In the M region, annual net carbon
625 uptake is less than in years 2017-2018, but it is within the range of LoFI climatology value
626 implying that the estimated NEE is not necessarily an extreme anomaly. For the S re-
627 gion, 2019 annual NEE is more negative than that in previous two years and LoFI cli-
628 matology, which can be mainly attributable to the enhanced net uptake in May of 2019
629 (Figure 10c) when the precipitation event had the most influence.

630 These identified features in the M and S regions could be inspected further by look-
631 ing at NEE budgets specifically for growing seasons. For the purpose of this study grow-
632 ing seasons are defined as a string of months with consistent negative NEE based upon
633 Figures 9-11. As such the following timeframes are identified: May-September for the
634 M region, April-September for the S region, and March-July for the T region. Figure 12
635 compares optimized NEE summed over a region for the years 2017-2019. The result is
636 similar to what was previously discussed with year 2019 in the M and S regions exhibit-
637 ing decreased and increased net uptakes respectively. In Figure 12 the impacts on NEE
638 appear more pronounced as only growing seasons are considered, which were affected by
639 the extreme precipitation more directly. Another important note to be made here is that
640 regional drought in 2018 did not affect the M region NEE as markedly as the flood of
641 2019. Relatively small carbon flux variation over the T region suggests that the corre-
642 sponding vegetation of grasslands and savannas is less affected by the anomalously wet
643 conditions. Adding up all the surveyed information in this work it can be concluded that
644 the extreme flooding of 2019 did affect NEE significantly in the M and S regions and more
645 so during the growing season when the consequences of the flood were most pronounced.

646 4 Conclusions

647 Generally prolonged excessive water conditions will negatively influence a plant sys-
648 tem causing anoxia (W. Zhou et al., 2020); however, the effects of flooding on an ecosys-
649 tem are not straightforward and largely depend on a particular vegetation type and de-
650 gree of waterlogging (Detmers et al., 2015; Sun et al., 2022). Wet conditions can result
651 in an increase of carbon net uptake, but too much wetness may lead to a net carbon re-
652 lease because in these conditions both productivity and respiration tend to decrease, and
653 the overall NEE balance will be contingent on specific environmental conditions (Ahlström

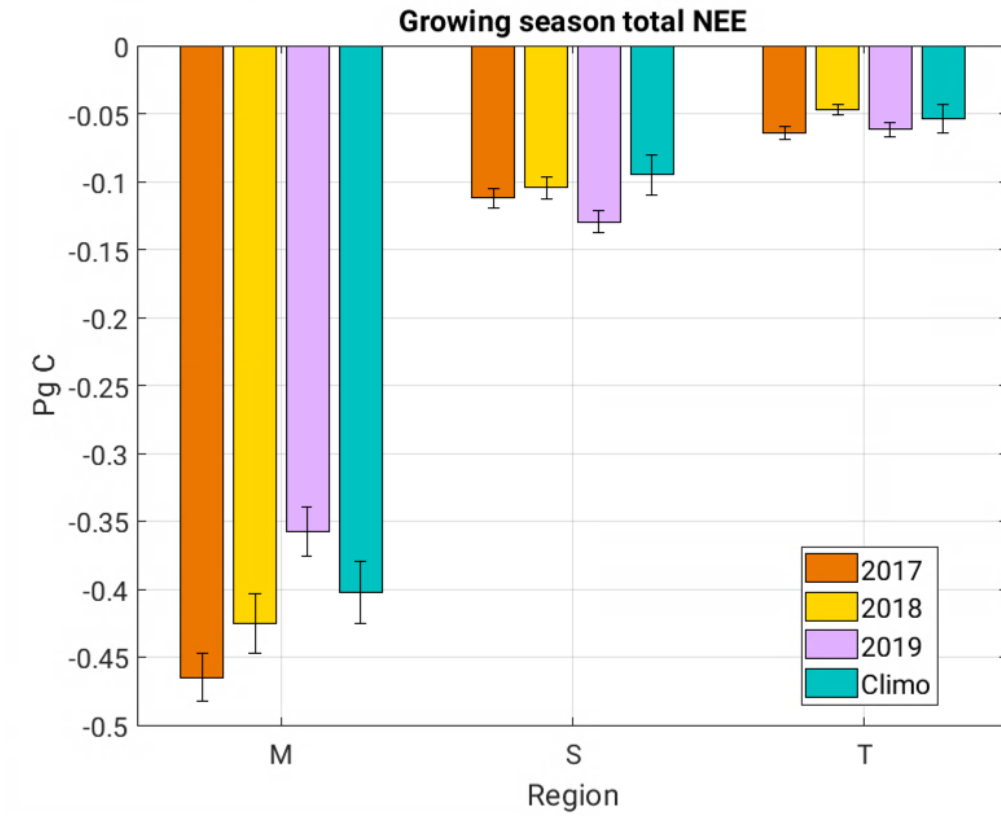


Figure 12. Optimized total growing season NEE for years 2017-2019 and corresponding LoFI 2000-2016 climatology as a function of a region. Growing seasons are defined as follows: May-September for the M region, April-September for the S region, and March-July for the T region.

654 et al., 2015; Bloch & Bhattacharjee, 2020). The current study affirms the mentioned as-
655 sertions and implies that crops such as corn and soybeans seem to be more susceptible
656 to waterlogging than non-crop vegetation such as savannas, forests, and grasslands. This
657 is expressed in the reduced carbon uptake in the first part of the growing season over
658 the Midwestern region of the US (mainly crops) and overall increased carbon uptake in
659 the Southern region of the US (mainly non-crop) during the flood of 2019 when compared
660 to 2017 and 2018. The change in 2019 annual NEE in the Midwest with respect to 2017
661 and 2018 of about 0.07 Pg C nearly equaled to the total magnitude of NEE in the re-
662 gions S and T in 2019 when it was at the highest value among the examined years (-0.1
663 Pg C). For the perspective, an annual average NEE over the years 2010-2019 in North
664 America is about -0.5 Pg C (Jiang et al., 2022). In addition, significant slowdown of the
665 crop planting progress occurred in the early growing season of 2019 as most of the corn
666 and soybeans in the US are in the Midwest. Flooding impacts in managed ecosystems
667 dominated the net effect for the 2019 event. As humans are considering a variety of strate-
668 gies to tackle climate change, sustainable crop management practice can accelerate car-
669 bon input into the soil (Meena et al., 2020). The exact effect of flooding on such prac-
670 tices is unclear but the delay in planting of crops explored in the current work raises ques-
671 tions that could influence future carbon balance and should be considered in strategies
672 to reduce net emissions.

673 The impact of flooding on NEE and atmospheric CO_2 is readily observed by satel-
674 lites (Yin et al., 2020) and a variety of insitu observational approaches (this study). Like
675 Yin et al. (2020)), for the Midwestern region this study finds a decrease in net carbon
676 uptake over June and July of 2019 of about 0.06-1.2 PgC [roughly 12-24% of an aver-
677 age annual carbon net uptake in North America (Jiang et al., 2022)] when compared to
678 both 2017 and 2018 and an increase in net carbon uptake in August and September of
679 near 0.05 PgC (roughly 10% of an average annual carbon net uptake in North America)
680 when compared to 2018 [Note that Yin et al. (2020) estimated Gross Primary Produc-
681 tion (GPP), which does not account for RE, while this study estimated NEE]. However,
682 the results from the current study suggest that comparing 2019 to 2018 may not be op-
683 timal as 2018 may not be representative of an average growing season carbon activity
684 (Jiang et al., 2022). For instance, assessment of 2019 NEE values with 2017 NEE val-
685 ues does not seem to show a “recovery” in August-September time frame as stated in Yin
686 et al. (2020) and Turner et al. (2021) suggesting that additional inquiries are required
687 into the detailed effects of flooding on the carbon uptake. Atmospheric CO_2 observations
688 can play an important role in helping to monitor the impact of agricultural systems but
689 require sustained planning and coordination (e.g., the discontinuity in towers made this
690 study more difficult).

691 Finally, the assessment of the GEOS LoFI model shows that the model can sim-
692 ulate large-scale variations of CO_2 with notable skill in the Midwest and parts of the South,
693 but some biases are evident. For instance, more uptake is required in the second part
694 of the summer across all the examined regions, while uptake generally tends to be too
695 high in May over the Midwest. These biases are consistent with Y. Zhou et al. (2020)
696 study, which evaluated CASA against flux towers and other ecosystem models. Given
697 that the GEOS LoFI is based on CASA such result is not surprising. Additionally, the
698 model struggled to replicate CO_2 during passages of frontal systems that appear as spikes
699 and dips in time series, specifically in the South. This could be attributable to the fact
700 that LoFI is a monthly product downscaled to provide daily fluxes, which lack the needed
701 resolution to accurately represent day to day variations in CO_2 (Weir et al., 2021).

702 Overall, the low latency flux estimation approach from LoFI is credible in discern-
703 ing flooding and non-flooding events, which demonstrates the maturity of modeling tools
704 that can be applied to carbon monitoring at the current stage. Further investigations
705 in this direction are imperative as only a sparse amount of literature is available regard-

ing carbon exchange between an ecosystem and the atmosphere in a variety of water-excess conditions.

5 Acknowledgements

This work is supported by NASA’s Carbon Monitoring System (NNH16DA001N-CMS 16-CMS16-0054, NNH20DA001N-CMS 20-CMS20-0011), NASA Postdoctoral Program (NPP), and a contract appointment with Earth System Science Interdisciplinary Center (ESSIC) at University of Maryland (UMD). We thank NASA Goddard Space Flight Center (GSFC) facility for providing us with the tools needed to perform the simulations used in this work. Also, we wish to thank ACT-America and Feasibility Study on Using Satellite-based Data for Offshore Air Quality Monitoring (SCOAPE) teams for helping us with specific questions pertinent to the data considered in the current study. Much gratitude to the reviewers who provided in-depth reviews that tremendously helped to improve the article.

6 Open Research

Data Availability Statement

CO₂ data from MS-01, MS-02, AL-01, and LA-01 towers are available at <https://sites.psu.edu/gulfcoast/data/>; also see Miles et al. (2018). WBI and WKT tower data are available here: <https://gml.noaa.gov/ccgg/obspack/index.html>. All of the crop data used in this article can be found at <https://quickstats.nass.usda.gov/>. ACT airborne data are located at https://actamerica.ornl.gov/airborne_data.shtml. SCOAPE data are stored at <https://www-air.larc.nasa.gov/missions/scoape/index.html>. MERRA-2 data used for GEOS forcing, precipitation and soil moisture analyzes are available at <https://gmao.gsfc.nasa.gov/reanalysis/MERRA-2/>. Source code for the NASA GEOS model is available under the NASA Open-Source Agreement at <http://opensource.gsfc.nasa.gov/projects/GEOS-5>. The NEE fluxes used in GEOS are based on the CASA-GFED dataset provided at GES DISC (https://disc.gsfc.nasa.gov/datasets/GEOS_CASAGFED_3H_NEE_3/summary).

More extensive descriptions of tower and airborne data can be found in Wei et al. (2021) and Masarie et al. (2014).

References

- Ahlström, A., Raupach, M. R., Schurgers, G., Smith, B., Arneeth, A., Jung, M., . . . Zeng, N. (2015). The dominant role of semi-arid ecosystems in the trend and variability of the land CO₂ sink. *Science*, *348*(6237), 895–899. Retrieved from <https://www.science.org/doi/abs/10.1126/science.aaa1668> doi: 10.1126/science.aaa1668
- Ahmed, F., Raffi, M., Ismail, M. R., Juraimi, A. S., Rahim, H., Asfaliza, R., & Latif, M. A. (2013). Waterlogging tolerance of crops: breeding, mechanism of tolerance, molecular approaches, and future prospects. *BioMed research international*, *2013*.
- Andrews, A. E., Kofler, J. D., Trudeau, M. E., Williams, J. C., Neff, D. H., Masarie, K. A., . . . Tans, P. P. (2014). CO₂, CO, and CH₄ measurements from tall towers in the noaa earth system research laboratory’s global greenhouse gas reference network: instrumentation, uncertainty analysis, and recommendations for future high-accuracy greenhouse gas monitoring efforts. *Atmospheric Measurement Techniques*, *7*(2), 647–687. Retrieved from <https://amt.copernicus.org/articles/7/647/2014/> doi: 10.5194/amt-7-647-2014

- 753 Bloch, M., & Bhattacharjee, J. (2020). Characterizing the carbon fluxes of a bot-
754 tom-land hardwood forest. In *Agu fall meeting abstracts* (Vol. 2020, pp. B065-
755 0004).
- 756 Bourtsoukidis, E., Kawaletz, H., Radacki, D., Schütz, S., Hakola, H., Hellén, H., ...
757 Bonn, B. (2014). Impact of flooding and drought conditions on the emission
758 of volatile organic compounds of quercus robur and prunus serotina. *Trees*,
759 *28*(1), 193–204.
- 760 Chevallier, F., Wang, T., Ciais, P., Maignan, F., Bocquet, M., Altaf Arain, M., ...
761 Moors, E. J. (2012). What eddy-covariance measurements tell us about prior
762 land flux errors in CO₂-flux inversion schemes. *Global Biogeochemical Cycles*,
763 *26*(1). Retrieved from [https://agupubs.onlinelibrary.wiley.com/doi/](https://agupubs.onlinelibrary.wiley.com/doi/abs/10.1029/2010GB003974)
764 [abs/10.1029/2010GB003974](https://doi.org/10.1029/2010GB003974) doi: <https://doi.org/10.1029/2010GB003974>
- 765 Dalmagro, H. J., Zanella de Arruda, P. H., Vourlitis, G. L., Lathuillière, M. J.,
766 de S. Nogueira, J., Couto, E. G., & Johnson, M. S. (2019). Radiative
767 forcing of methane fluxes offsets net carbon dioxide uptake for a tropical
768 flooded forest. *Global Change Biology*, *25*(6), 1967–1981. Retrieved from
769 <https://onlinelibrary.wiley.com/doi/abs/10.1111/gcb.14615> doi:
770 <https://doi.org/10.1111/gcb.14615>
- 771 Davis, K. J., Browell, E. V., Feng, S., Lauvaux, T., Obland, M. D., Pal, S., ...
772 Williams, C. A. (2021). The atmospheric carbon and transport (ACT)-america
773 mission. *Bulletin of the American Meteorological Society*, *102*(9), E1714 -
774 E1734. Retrieved from [https://journals.ametsoc.org/view/journals/](https://journals.ametsoc.org/view/journals/bams/102/9/BAMS-D-20-0300.1.xml)
775 [bams/102/9/BAMS-D-20-0300.1.xml](https://doi.org/10.1175/BAMS-D-20-0300.1) doi: [10.1175/BAMS-D-20-0300.1](https://doi.org/10.1175/BAMS-D-20-0300.1)
- 776 Davis, K. J., Deng, A., Lauvaux, T., Miles, N. L., Richardson, S. J., Sarmiento,
777 D. P., ... Karion, A. (2017, 05). The Indianapolis Flux Experiment (IN-
778 FLUX): A test-bed for developing urban greenhouse gas emission mea-
779 surements. *Elementa: Science of the Anthropocene*, *5*. Retrieved from
780 <https://doi.org/10.1525/elementa.188> (21) doi: [10.1525/elementa.188](https://doi.org/10.1525/elementa.188)
- 781 Detmers, R. G., Hasekamp, O., Aben, I., Houweling, S., van Leeuwen, T. T., Butz,
782 A., ... Poulter, B. (2015). Anomalous carbon uptake in australia as seen
783 by GOSAT. *Geophysical Research Letters*, *42*(19), 8177–8184. Retrieved
784 from [https://agupubs.onlinelibrary.wiley.com/doi/abs/10.1002/](https://agupubs.onlinelibrary.wiley.com/doi/abs/10.1002/2015GL065161)
785 [2015GL065161](https://doi.org/10.1002/2015GL065161) doi: <https://doi.org/10.1002/2015GL065161>
- 786 Dinsmore, K. J., Billett, M. F., & Dyson, K. E. (2013). Temperature and precip-
787 itation drive temporal variability in aquatic carbon and ghg concentrations
788 and fluxes in a peatland catchment. *Global Change Biology*, *19*(7), 2133-
789 2148. Retrieved from [https://onlinelibrary.wiley.com/doi/abs/10.1111/](https://onlinelibrary.wiley.com/doi/abs/10.1111/gcb.12209)
790 [gcb.12209](https://doi.org/10.1111/gcb.12209) doi: <https://doi.org/10.1111/gcb.12209>
- 791 Dlugokencky, E., & Tans, P. (2016). *The marine boundary layer reference (down-*
792 *loaded early 2016)*.
- 793 Dušek, J., Čížková, H., Czerný, R., Taufarová, K., Šmídová, M., & Janouš, D.
794 (2009). Influence of summer flood on the net ecosystem exchange of CO₂
795 in a temperate sedge-grass marsh. *Agricultural and Forest Meteorology*,
796 *149*(9), 1524–1530. Retrieved from [https://www.sciencedirect.com/](https://www.sciencedirect.com/science/article/pii/S0168192309000951)
797 [science/article/pii/S0168192309000951](https://doi.org/10.1016/j.agrformet.2009.04.007) doi: [https://doi.org/10.1016/](https://doi.org/10.1016/j.agrformet.2009.04.007)
- 798 [j.agrformet.2009.04.007](https://doi.org/10.1016/j.agrformet.2009.04.007)
- 799 Follett, R. (2001). Soil management concepts and carbon sequestration in crop-
800 land soils. *Soil and Tillage Research*, *61*(1), 77–92. Retrieved from [https://](https://www.sciencedirect.com/science/article/pii/S0167198701001805)
801 [www.sciencedirect.com/science/article/pii/S0167198701001805](https://doi.org/10.1016/S0167-1987(01)00180-5) (XVth
802 ISTRO Conference on Tillage at the Threshold of the 21st Century: Looking
803 Ahead) doi: [https://doi.org/10.1016/S0167-1987\(01\)00180-5](https://doi.org/10.1016/S0167-1987(01)00180-5)
- 804 Frank, D., Reichstein, M., Bahn, M., Thonicke, K., Frank, D., Mahecha, M. D., ...
805 Zscheischler, J. (2015). Effects of climate extremes on the terrestrial carbon
806 cycle: concepts, processes and potential future impacts. *Global Change Biol-*
807 *ogy*, *21*(8), 2861–2880. Retrieved from <https://onlinelibrary.wiley.com/>

- 808 doi/abs/10.1111/gcb.12916 doi: <https://doi.org/10.1111/gcb.12916>
- 809 Friend, A. D., ARNETH, A., KIANG, N. Y., LOMAS, M., OGÉE, J., RÖDEN-
810 BECK, C., ... ZAEHLE, S. (2007). Fluxnet and modelling the global carbon
811 cycle. *Global Change Biology*, 13(3), 610-633. Retrieved from [https://
812 onlinelibrary.wiley.com/doi/abs/10.1111/j.1365-2486.2006.01223.x](https://onlinelibrary.wiley.com/doi/abs/10.1111/j.1365-2486.2006.01223.x)
813 doi: <https://doi.org/10.1111/j.1365-2486.2006.01223.x>
- 814 Gelaro, R., McCarty, W., Suárez, M. J., Todling, R., Molod, A., Takacs, L., ...
815 Zhao, B. (2017). The modern-era retrospective analysis for research and ap-
816 plications, version 2 (MERRA-2). *Journal of Climate*, 30(14), 5419 - 5454.
817 Retrieved from [https://journals.ametsoc.org/view/journals/clim/30/
818 14/jcli-d-16-0758.1.xml](https://journals.ametsoc.org/view/journals/clim/30/14/jcli-d-16-0758.1.xml) doi: 10.1175/JCLI-D-16-0758.1
- 819 Guanter, L., Zhang, Y., Jung, M., Joiner, J., Voigt, M., Berry, J. A., ... Griffis,
820 T. J. (2014). Global and time-resolved monitoring of crop photosynthesis with
821 chlorophyll fluorescence. *Proceedings of the National Academy of Sciences*,
822 111(14), E1327-E1333. Retrieved from [https://www.pnas.org/doi/abs/
823 10.1073/pnas.1320008111](https://www.pnas.org/doi/abs/10.1073/pnas.1320008111) doi: 10.1073/pnas.1320008111
- 824 Haigh, T. R., Otkin, J. A., Woloszyn, M., Todey, D., & Felkley, C. (2022). Meeting
825 the drought information needs of midwest perennial specialty crop produc-
826 ers. *Journal of Applied Meteorology and Climatology*, 61(7), 839 - 855. Re-
827 trieved from [https://journals.ametsoc.org/view/journals/apme/61/7/
828 JAMC-D-21-0105.1.xml](https://journals.ametsoc.org/view/journals/apme/61/7/JAMC-D-21-0105.1.xml) doi: <https://doi.org/10.1175/JAMC-D-21-0105.1>
- 829 Han, G., Chu, X., Xing, Q., Li, D., Yu, J., Luo, Y., ... Rafique, R. (2015).
830 Effects of episodic flooding on the net ecosystem CO₂ exchange of a
831 supratidal wetland in the yellow river delta. *Journal of Geophysical Re-
832 search: Biogeosciences*, 120(8), 1506-1520. Retrieved from [https://
833 agupubs.onlinelibrary.wiley.com/doi/abs/10.1002/2015JG002923](https://agupubs.onlinelibrary.wiley.com/doi/abs/10.1002/2015JG002923) doi:
834 <https://doi.org/10.1002/2015JG002923>
- 835 Heald, C. L., Jacob, D. J., Jones, D. B. A., Palmer, P. I., Logan, J. A., Streets,
836 D. G., ... Nehr Korn, T. (2004). Comparative inverse analysis of satellite
837 (mopitt) and aircraft (trace-p) observations to estimate asian sources of car-
838 bon monoxide. *Journal of Geophysical Research: Atmospheres*, 109(D23).
839 Retrieved from [https://agupubs.onlinelibrary.wiley.com/doi/abs/
840 10.1029/2004JD005185](https://agupubs.onlinelibrary.wiley.com/doi/abs/10.1029/2004JD005185) doi: <https://doi.org/10.1029/2004JD005185>
- 841 Hilton, R. G., Galy, A., Hovius, N., Chen, M.-C., Horng, M.-J., & Chen, H. (2008).
842 Tropical-cyclone-driven erosion of the terrestrial biosphere from mountains. *na-
843 ture Geoscience*, 1(11), 759-762.
- 844 Jiang, F., Ju, W., He, W., Wu, M., Wang, H., Wang, J., ... Chen, J. M. (2022). A
845 10-year global monthly averaged terrestrial net ecosystem exchange dataset in-
846 ferred from the ACOS GOSAT v9 XCO₂ retrievals (GCAS2021). *Earth System
847 Science Data*, 14(7), 3013-3037. Retrieved from [https://essd.copernicus
848 .org/articles/14/3013/2022/](https://essd.copernicus.org/articles/14/3013/2022/) doi: 10.5194/essd-14-3013-2022
- 849 Knapp, A. K., Beier, C., Briske, D. D., Classen, A. T., Luo, Y., Reichstein, M., ...
850 Weng, E. (2008, 10). Consequences of More Extreme Precipitation Regimes
851 for Terrestrial Ecosystems. *BioScience*, 58(9), 811-821. Retrieved from
852 <https://doi.org/10.1641/B580908> doi: 10.1641/B580908
- 853 Koster, R. D., Darmenov, A. S., & da Silva, A. M. (2015). *The quick fire emissions
854 dataset (QFED): Documentation of versions 2.1, 2.2 and 2.4* (Tech. Rep.).
- 855 Kramer, K., Vreugdenhil, S. J., & van der Werf, D. (2008). Effects of flooding on
856 the recruitment, damage and mortality of riparian tree species: A field and
857 simulation study on the rhine floodplain. *Forest Ecology and Management*,
858 255(11), 3893-3903. Retrieved from [https://www.sciencedirect.com/
859 science/article/pii/S0378112708002922](https://www.sciencedirect.com/science/article/pii/S0378112708002922) doi: [https://doi.org/10.1016/
860 j.foreco.2008.03.044](https://doi.org/10.1016/j.foreco.2008.03.044)
- 861 Lal, R. (2019). Accelerated soil erosion as a source of atmospheric CO₂. *Soil and
862 Tillage Research*, 188, 35-40. Retrieved from <https://www.sciencedirect>

- 863 .com/science/article/pii/S0167198718300345 (Soil Carbon and Cli-
 864 mate Change: the 4 per Mille Initiative) doi: [https://doi.org/10.1016/](https://doi.org/10.1016/j.still.2018.02.001)
 865 [j.still.2018.02.001](https://doi.org/10.1016/j.still.2018.02.001)
- 866 Los, S. O., Pollack, N. H., Parris, M. T., Collatz, G. J., Tucker, C. J., Sellers,
 867 P. J., ... Dazlich, D. A. (2000). A global 9-yr biophysical land surface
 868 dataset from noaa avhrr data. *Journal of Hydrometeorology*, 1(2), 183 -
 869 199. Retrieved from [https://journals.ametsoc.org/view/journals/](https://journals.ametsoc.org/view/journals/hydr/1/2/1525-7541_2000_001_0183_agybls_2_0_co_2.xml)
 870 [hydr/1/2/1525-7541_2000_001_0183_agybls_2_0_co_2.xml](https://journals.ametsoc.org/view/journals/hydr/1/2/1525-7541_2000_001_0183_agybls_2_0_co_2.xml) doi:
 871 [https://doi.org/10.1175/1525-7541\(2000\)001<0183:AGYBLS>2.0.CO;2](https://doi.org/10.1175/1525-7541(2000)001<0183:AGYBLS>2.0.CO;2)
- 872 Ma, X., Huete, A., Cleverly, J., Eamus, D., Chevallier, F., Joiner, J., ... others
 873 (2016). Drought rapidly diminishes the large net co2 uptake in 2011 over
 874 semi-arid australia. *Scientific Reports*, 6(1), 37747.
- 875 Masarie, K. A., Peters, W., Jacobson, A. R., & Tans, P. P. (2014). Obspack:
 876 a framework for the preparation, delivery, and attribution of atmospheric
 877 greenhouse gas measurements. *Earth System Science Data*, 6(2), 375–384.
 878 Retrieved from <https://essd.copernicus.org/articles/6/375/2014/> doi:
 879 [10.5194/essd-6-375-2014](https://doi.org/10.5194/essd-6-375-2014)
- 880 Masarie, K. A., & Tans, P. P. (1995). Extension and integration of atmospheric
 881 carbon dioxide data into a globally consistent measurement record. *Journal*
 882 *of Geophysical Research: Atmospheres*, 100(D6), 11593-11610. Retrieved from
 883 <https://agupubs.onlinelibrary.wiley.com/doi/abs/10.1029/95JD00859>
 884 doi: <https://doi.org/10.1029/95JD00859>
- 885 Meena, R. S., Kumar, S., & Yadav, G. S. (2020). Soil carbon sequestration in crop
 886 production. In R. S. Meena (Ed.), *Nutrient dynamics for sustainable crop pro-*
 887 *duction* (pp. 1–39). Singapore: Springer Singapore. Retrieved from [https://](https://doi.org/10.1007/978-981-13-8660-2_1)
 888 doi.org/10.1007/978-981-13-8660-2_1 doi: 10.1007/978-981-13-8660-2_1
- 889 Miles, N., Richardson, S., Martins, D., Davis, K., Lauvaux, T., Haupt, B., & Miller,
 900 S. (2018). *Act-america: L2 in situ CO₂, CO, and CH₄ concentrations from*
 901 *towers, eastern USA. ornl daac, oak ridge, tennessee, usa.*
- 892 Miyata, A., Leuning, R., Denmead, O. T., Kim, J., & Harazono, Y. (2000). Carbon
 893 dioxide and methane fluxes from an intermittently flooded paddy field. *Agri-*
 894 *cultural and Forest Meteorology*, 102(4), 287-303. Retrieved from [https://](https://www.sciencedirect.com/science/article/pii/S0168192300000927)
 895 www.sciencedirect.com/science/article/pii/S0168192300000927 doi:
 896 [https://doi.org/10.1016/S0168-1923\(00\)00092-7](https://doi.org/10.1016/S0168-1923(00)00092-7)
- 897 Molod, A., Takacs, L., Suarez, M., & Bacmeister, J. (2015). Development of the
 898 GEOS-5 atmospheric general circulation model: evolution from MERRA
 899 to MERRA2. *Geoscientific Model Development*, 8(5), 1339–1356. Re-
 900 trieved from <https://gmd.copernicus.org/articles/8/1339/2015/> doi:
 901 [10.5194/gmd-8-1339-2015](https://doi.org/10.5194/gmd-8-1339-2015)
- 902 National Centers for Environmental Information. (2018). *Assessing the u.s. climate*
 903 *in september 2018.* (Available at [https://www.ncei.noaa.gov/news/national-](https://www.ncei.noaa.gov/news/national-climate-201809)
 904 [climate-201809](https://www.ncei.noaa.gov/news/national-climate-201809). Accessed April 2 2023)
- 905 Neri, A., Villarini, G., & Napolitano, F. (2020). Intraseasonal predictability of the
 906 duration of flooding above national weather service flood warning levels across
 907 the U.S. midwest. *Hydrological Processes*, 34(23), 4505-4511. Retrieved from
 908 <https://onlinelibrary.wiley.com/doi/abs/10.1002/hyp.13902> doi:
 909 <https://doi.org/10.1002/hyp.13902>
- 910 Oda, T., & Maksyutov, S. (2015). ODIAC fossil fuel CO₂ emissions dataset (version
 911 name: ODIAC2016). *Center for Global Environmental Research, National In-*
 912 *stitute for Environmental Studies*, <https://doi.org/10.17595/20170411.001>.
- 913 Oda, T., Maksyutov, S., & Andres, R. J. (2018). The open-source data inven-
 914 tory for anthropogenic co₂, version 2016 (odiac2016): a global monthly fossil
 915 fuel co₂ gridded emissions data product for tracer transport simulations and
 916 surface flux inversions. *Earth System Science Data*, 10(1), 87–107. Re-
 917 trieved from <https://essd.copernicus.org/articles/10/87/2018/> doi:

- 10.5194/essd-10-87-2018
- Ott, L. E., Pawson, S., Collatz, G. J., Gregg, W. W., Menemenlis, D., Brix, H., ...
 Kawa, S. R. (2015). Assessing the magnitude of CO₂ flux uncertainty in
 atmospheric CO₂ records using products from nasa's carbon monitoring flux
 pilot project. *Journal of Geophysical Research: Atmospheres*, 120(2), 734–
 765. Retrieved from <https://agupubs.onlinelibrary.wiley.com/doi/abs/10.1002/2014JD022411> doi: <https://doi.org/10.1002/2014JD022411>
- Paustian, K., Six, J., Elliott, E., & Hunt, H. (2000). Management options for reduc-
 ing CO₂ emissions from agricultural soils. *Biogeochemistry*, 48(1), 147–163.
- Price, J. J., & Berkowitz, J. F. (2020). Wetland functional responses to prolonged
 inundation in the active mississippi river floodplain. *Wetlands*, 40(6), 1949–
 1956.
- Randerson, J. T., Thompson, M. V., Malmstrom, C. M., Field, C. B., & Fung,
 I. Y. (1996). Substrate limitations for heterotrophs: Implications for models
 that estimate the seasonal cycle of atmospheric CO₂. *Global Biogeochemical
 Cycles*, 10(4), 585–602. Retrieved from <https://agupubs.onlinelibrary.wiley.com/doi/abs/10.1029/96GB01981> doi: <https://doi.org/10.1029/96GB01981>
- Reed, T., Mason, L. R., & Ekenga, C. C. (2020). Adapting to climate change
 in the upper mississippi river basin: Exploring stakeholder perspectives on
 river system management and flood risk reduction. *Environmental Health In-
 sights*, 14, 1178630220984153. Retrieved from <https://doi.org/10.1177/1178630220984153> (PMID: 33447043) doi: 10.1177/1178630220984153
- Reichle, R. H., Draper, C. S., Liu, Q., Giroto, M., Mahanama, S. P., Koster, R. D.,
 & De Lannoy, G. J. (2017). Assessment of MERRA-2 land surface hydrology
 estimates. *Journal of Climate*, 30(8), 2937–2960.
- Reichle, R. H., Liu, Q., Koster, R. D., Draper, C. S., Mahanama, S. P., & Partyka,
 G. S. (2017). Land surface precipitation in MERRA-2. *Journal of Climate*,
 30(5), 1643–1664.
- Reichstein, M., Bahn, M., Ciais, P., Frank, D., Mahecha, M. D., Seneviratne, S. I.,
 ... others (2013). Climate extremes and the carbon cycle. *Nature*, 500(7462),
 287–295.
- Rodgers, C. D. (2000). *Inverse methods for atmospheric sounding: theory and prac-
 tice* (Vol. 2). World scientific.
- Rosenzweig, C., Tubiello, F. N., Goldberg, R., Mills, E., & Bloomfield, J. (2002). In-
 creased crop damage in the us from excess precipitation under climate change.
Global Environmental Change, 12(3), 197–202. Retrieved from <https://www.sciencedirect.com/science/article/pii/S0959378002000080> doi:
[https://doi.org/10.1016/S0959-3780\(02\)00008-0](https://doi.org/10.1016/S0959-3780(02)00008-0)
- Schuldt, K. N., Mund, M., Luijkx, I. T., Aalto, T., Abshire, J. B., Aikin, K., ...
 others (2021). Multi-laboratory compilation of atmospheric carbon dioxide
 data for the period 1957–2019, obspack_co2_1_GLOBALVIEWplus_v6.
 1_2021-03-01, NOAA earth system research laboratory, global monitoring
 laboratory [data set]. *NOAA Earth System Research Laboratory, Global Moni-
 toring Laboratory [data set]*, 10, 20210801.
- Schwalm, C. R., Williams, C. A., Schaefer, K., Baldocchi, D., Black, T. A., Gold-
 stein, A. H., ... Scott, R. L. (2012). Reduction in carbon uptake during turn
 of the century drought in western north america. *Nature Geoscience*, 5(8),
 551–556.
- Stein, A. F., Draxler, R. R., Rolph, G. D., Stunder, B. J. B., Cohen, M. D., & Ngan,
 F. (2015). NOAA's HYSPLIT atmospheric transport and dispersion modeling
 system. *Bulletin of the American Meteorological Society*, 96(12), 2059 - 2077.
 Retrieved from [https://journals.ametsoc.org/view/journals/bams/96/
 12/bams-d-14-00110.1.xml](https://journals.ametsoc.org/view/journals/bams/96/12/bams-d-14-00110.1.xml) doi: 10.1175/BAMS-D-14-00110.1
- Sulla-Menashe, D., & Friedl, M. A. (2018). User guide to collection 6 MODIS land

- 973 cover (MCD12q1 and MCD12C1) product. *USGS: Reston, VA, USA, 1*, 18.
- 974 Sun, B., Jiang, M., Han, G., Zhang, L., Zhou, J., Bian, C., ... Xia, J. (2022).
 975 Experimental warming reduces ecosystem resistance and resilience to se-
 976 vere flooding in a wetland. *Science Advances*, 8(4), eabl9526. Retrieved
 977 from <https://www.science.org/doi/abs/10.1126/sciadv.abl9526> doi:
 978 10.1126/sciadv.abl9526
- 979 Turner, A. J., Köhler, P., Magney, T. S., Frankenberg, C., Fung, I., & Cohen,
 980 R. C. (2021). Extreme events driving year-to-year differences in gross pri-
 981 mary productivity across the us. *Biogeosciences*, 18(24), 6579–6588. Re-
 982 trieved from <https://bg.copernicus.org/articles/18/6579/2021/> doi:
 983 10.5194/bg-18-6579-2021
- 984 van der Molen, M., Dolman, A., Ciais, P., Eglin, T., Gobron, N., Law, B., ...
 985 Wang, G. (2011). Drought and ecosystem carbon cycling. *Agricul-
 986 tural and Forest Meteorology*, 151(7), 765–773. Retrieved from [https://
 987 www.sciencedirect.com/science/article/pii/S0168192311000517](https://www.sciencedirect.com/science/article/pii/S0168192311000517) doi:
 988 <https://doi.org/10.1016/j.agrformet.2011.01.018>
- 989 van der Werf, G. R., Randerson, J. T., Giglio, L., Collatz, G. J., Mu, M., Kasib-
 990 hatla, P. S., ... van Leeuwen, T. T. (2010). Global fire emissions and the
 991 contribution of deforestation, savanna, forest, agricultural, and peat fires
 992 (1997–2009). *Atmospheric Chemistry and Physics*, 10(23), 11707–11735.
 993 Retrieved from <https://acp.copernicus.org/articles/10/11707/2010/>
 994 doi: 10.5194/acp-10-11707-2010
- 995 Wei, Y., Shrestha, R., Pal, S., Gerken, T., Feng, S., McNelis, J., ... Davis, K. J.
 996 (2021). Atmospheric carbon and transport – america (ACT-america) data
 997 sets: Description, management, and delivery. *Earth and Space Science*, 8(7),
 998 e2020EA001634. Retrieved from [https://agupubs.onlinelibrary.wiley
 999 .com/doi/abs/10.1029/2020EA001634](https://agupubs.onlinelibrary.wiley.com/doi/abs/10.1029/2020EA001634) (e2020EA001634 2020EA001634) doi:
 1000 <https://doi.org/10.1029/2020EA001634>
- 1001 Weir, B., Ott, L. E., Collatz, G. J., Kawa, S. R., Poulter, B., Chatterjee, A.,
 1002 ... Pawson, S. (2021). Bias-correcting carbon fluxes derived from land-
 1003 surface satellite data for retrospective and near-real-time assimilation sys-
 1004 tems. *Atmospheric Chemistry and Physics*, 21(12), 9609–9628. Retrieved
 1005 from <https://acp.copernicus.org/articles/21/9609/2021/> doi:
 1006 10.5194/acp-21-9609-2021
- 1007 Yildirim, E., & Demir, I. (2022). Agricultural flood vulnerability assessment and
 1008 risk quantification in iowa. *Science of The Total Environment*, 826, 154165.
 1009 Retrieved from [https://www.sciencedirect.com/science/article/pii/
 1010 S0048969722012578](https://www.sciencedirect.com/science/article/pii/S0048969722012578) doi: <https://doi.org/10.1016/j.scitotenv.2022.154165>
- 1011 Yin, Y., Byrne, B., Liu, J., Wennberg, P. O., Davis, K. J., Magney, T., ... Franken-
 1012 berg, C. (2020). Cropland carbon uptake delayed and reduced by 2019 mid-
 1013 west floods. *AGU Advances*, 1(1), e2019AV000140. Retrieved from [https://
 1014 agupubs.onlinelibrary.wiley.com/doi/abs/10.1029/2019AV000140](https://agupubs.onlinelibrary.wiley.com/doi/abs/10.1029/2019AV000140)
 1015 (e2019AV000140 2019AV000140) doi: <https://doi.org/10.1029/2019AV000140>
- 1016 Zaerr, J. B. (1983, 03). Short-Term Flooding and Net Photosynthesis in Seedlings
 1017 of Three Conifers. *Forest Science*, 29(1), 71–78. Retrieved from [https://doi
 1018 .org/10.1093/forestscience/29.1.71](https://doi.org/10.1093/forestscience/29.1.71) doi: 10.1093/forestscience/29.1.71
- 1019 Zhang, W., & Villarini, G. (2021). Greenhouse gases drove the increasing trends in
 1020 spring precipitation across the central USA. *Philosophical Transactions of the
 1021 Royal Society A: Mathematical, Physical and Engineering Sciences*, 379(2195),
 1022 20190553. Retrieved from [https://royalsocietypublishing.org/doi/abs/
 1023 10.1098/rsta.2019.0553](https://royalsocietypublishing.org/doi/abs/10.1098/rsta.2019.0553) doi: 10.1098/rsta.2019.0553
- 1024 Zhou, W., Chen, F., Meng, Y., Chandrasekaran, U., Luo, X., Yang, W., & Shu,
 1025 K. (2020). Plant waterlogging/flooding stress responses: From seed ger-
 1026 mination to maturation. *Plant Physiology and Biochemistry*, 148, 228–236.
 1027 Retrieved from <https://www.sciencedirect.com/science/article/pii/>

- 1028 S0981942820300206 doi: <https://doi.org/10.1016/j.plaphy.2020.01.020>
1029 Zhou, Y., Williams, C. A., Lauvaux, T., Davis, K. J., Feng, S., Baker, I., . . . Wei, Y.
1030 (2020). A multiyear gridded data ensemble of surface biogenic carbon fluxes for
1031 north america: Evaluation and analysis of results. *Journal of Geophysical Re-*
1032 *search: Biogeosciences*, 125(2), e2019JG005314. Retrieved from [https://](https://agupubs.onlinelibrary.wiley.com/doi/abs/10.1029/2019JG005314)
1033 agupubs.onlinelibrary.wiley.com/doi/abs/10.1029/2019JG005314
1034 (e2019JG005314 2019JG005314) doi: <https://doi.org/10.1029/2019JG005314>
1035 Zomer, R. J., Bossio, D. A., Sommer, R., & Verchot, L. V. (2017). Global sequestra-
1036 tion potential of increased organic carbon in cropland soils. *Scientific Reports*,
1037 7(1), 1–8.
1038 Zona, D., Lipson, D. A., Paw U, K. T., Oberbauer, S. F., Olivas, P., Gioli, B., &
1039 Oechel, W. C. (2012). Increased CO₂ loss from vegetated drained lake
1040 tundra ecosystems due to flooding. *Global Biogeochemical Cycles*, 26(2).
1041 Retrieved from [https://agupubs.onlinelibrary.wiley.com/doi/abs/](https://agupubs.onlinelibrary.wiley.com/doi/abs/10.1029/2011GB004037)
1042 [10.1029/2011GB004037](https://agupubs.onlinelibrary.wiley.com/doi/abs/10.1029/2011GB004037) doi: <https://doi.org/10.1029/2011GB004037>